

s-Process Nucleosynthesis in Advanced Burning Phases of Massive Stars

Lih-Sin The¹, Mounib F. El Eid^{2,1}, and Bradley S. Meyer¹

ABSTRACT

We present a detailed study of s-process nucleosynthesis in massive stars of solar-like initial composition and masses 15, 20, 25, and 30 M_{\odot} . We update our previous results of s-process nucleosynthesis during the core He-burning of these stars and then focus on an analysis of the s-process under the physical conditions encountered during the shell-carbon burning. We show that the recent compilation of the $^{22}\text{Ne}(\alpha, n)^{25}\text{Mg}$ rate leads to a remarkable reduction of the efficiency of the s-process during core He-burning. In particular, this rate leads to the lowest overproduction factor of ^{80}Kr found to date during core He-burning in massive stars. The s-process yields resulting from shell carbon burning turn out to be very sensitive to the structural evolution of the carbon shell. This structure is influenced by the mass fraction of ^{12}C attained at the end of core helium burning, which in turn is mainly determined by the $^{12}\text{C}(\alpha, \gamma)^{16}\text{O}$ reaction. The still present uncertainty in the rate for this reaction implies that the s-process in massive stars is also subject to this uncertainty. We identify some isotopes like ^{70}Zn and ^{87}Rb as the signatures of the s-process during shell carbon burning in massive stars. In determining the relative contribution of our s-only stellar yields to the solar abundances, we find it is important to take into account the neutron exposure of shell carbon burning. When we analyze our yields with a Salpeter Initial Mass Function, we find that massive stars contribute at least 40% to s-only nuclei with mass $A \leq 87$. For s-only nuclei with mass $A > 90$, massive stars contribute on average $\sim 7\%$, except for ^{152}Gd , ^{187}Os , and ^{198}Hg which are $\sim 14\%$, $\sim 13\%$, and $\sim 11\%$, respectively.

Subject headings: nuclear reactions, nucleosynthesis, abundances—stars:evolution—stars: interiors

¹Department of Physics and Astronomy, Clemson University, Clemson, SC 29634-0978, tlihsin@clemson.edu; mbradle@clemson.edu

²Department of Physics, American University of Beirut, Beirut, Lebanon; meid@aub.edu.lb

1. Introduction

The s-process nucleosynthesis is the slow neutron-capture process of heavy nuclei in which the neutron-capture rate is slow relative to the beta-decay rate of the heavy nuclei near the line of beta stability (Burbidge et al. 1957; Cameron 1957). In this scenario, the seeds to synthesize the heavy nuclei are the iron-group nuclei. It is well known that massive stars of masses above $M \simeq 12M_{\odot}$ are the sites of the so-called “weak component” of s-process nucleosynthesis. The nuclei produced in this site are restricted to the atomic mass range $A \simeq 65-90$ (Kappeler et al. 1989; Busso et al. 1999). Many papers have explored this weak component of the s-process, but mainly during the core He-burning phase (Prantzos et al. 1987; Langer et al. 1989; Prantzos et al. 1990; Raiteri et al. 1991a; Baraffe et al. 1992; Rayet & Hashimoto 2000; The et al. 2000; El Eid et al. 2004). Few papers have investigated the s-process during the late evolution phases of massive stars, especially during the phase of shell carbon-burning (for short: shell C-burning) in these stars (Langer et al. 1989; Raiteri et al. 1991b, 1993). The study of the s-process during shell C-burning requires special effort, because this burning episode lasts until the end of a massive star’s evolution, as indicated by many works dealing with the advanced burning phases of massive stars (Nomoto & Hashimoto 1988; Chieffi et al. 1998; Limongi et al. 2000; Woosley et al. 2002; El Eid et al. 2004).

The contribution of the carbon shell to the s-process is important because the nuclei synthesized in this site will be eventually ejected largely unmodified during a supernova explosion of the star due to the lack of a neutron source during the explosive burning. Raiteri et al. (1993) argued on the basis of the calculations by Nomoto & Hashimoto (1988) that only stars of mass about $25 M_{\odot}$ are able to eject the s-nuclei synthesized in the C-shell. We further quantify this issue in §5. However, our main goal is to present a detailed study of the s-process during core He-burning and shell C-burning, thereby emphasizing the physical uncertainties influencing the results. We will benefit from our detailed calculations (El Eid et al. 2004, hereafter EMT04), where we have investigated the influence of several important physical quantities on the characteristics of the stellar models during the advanced burning phases of massive stars.

In §2, we summarize the main features of our previous stellar evolution calculations, which we have carried through the end of central oxygen burning. In §3, we present our updated results of the s-process during core He-burning. In §4, we present the characteristics of shell C-burning and discuss the results obtained for the s-process during shell C-burning. In §5 we show the location (as function of the interior radius) where nuclei are exposed to neutrons. In this section, we also show the effectiveness of neutron captures in producing heavy elements by calculating the total neutron capture in the stellar models. In §6 we

compare the production factor distribution of s-only nuclei from our stellar models with the distribution from the solar abundance. In §7 and in 8 we discuss and summarize the main conclusions of this paper.

2. Stellar Models

The results of the s-process presented in this paper have been obtained by using stellar models described in our previous paper (EMT04) for stars of masses 15, 20, 25, and 30 M_{\odot} with initial solar-like composition. We evolved our models beyond core oxygen burning, and this allows us to investigate the s-process nucleosynthesis not only during core He-burning, but also during the important phase of shell C-burning. The network we have used for the s-process is listed in Table 1 of The et al. (2000, hereafter TEM00). It includes 632 nuclei up to ^{210}Bi and is sufficiently inclusive that the s-process nucleosynthesis can be studied in detail. The sources of the important nuclear reaction rates for each studied model are summarized in Table 1. The nuclear data have been updated as follows:

1. The nuclear masses were taken from the compilation by Audi & Wapstra (1995)
2. The thermonuclear reaction rates were taken from the compilation of the “NACRE” collaboration (Angulo et al. 1999), and the “Non-Smoker” rates according to Rauscher & Thielemann (2000). Most of the electron capture and β -decay rates (referred to as weak interaction rates) are taken from Tuli (1995). Certain weak interaction rates are temperature and density dependent. These rates were taken from Takahashi & Yokoi (1987). However, we had to extrapolate some of the weak interaction rates (e.g., the β -decay rate of ^{79}Se) to higher temperatures based on experimental results by Klay & Käppeler (1988). We have also used some of the extrapolated data given by Raiteri et al. (1993) in their Table 2.
3. In our previous evolutionary calculations (EMT04), we investigated the effect of two different $^{12}\text{C}(\alpha, \gamma)^{16}\text{O}$ reaction rates: the NACRE rate and that due to Kunz et al. (2002). The first rate is larger than the second in the temperature range $T=(1-4)\times 10^8$ K (Fig. 1 of EMT04), which is relevant to core He-burning in the massive stars under consideration. However, Buchmann (1996) recommends a rate that is close to the rate given by Kunz et al. (2002) at temperature $T_9 \leq 0.4$ but is significantly larger at temperature range of $0.4 \leq T_9 \leq 3.0$. These different rates lead to several consequences during the late stage of core He-burning and also beyond this phase as described by EMT04. Here, we summarize some of the consequences that are relevant to the present study of the s-process.

In particular, using two different rates of the $^{12}\text{C}(\alpha, \gamma)^{16}\text{O}$ reaction in a $25 M_{\odot}$ star of initial solar-like composition, we found in the case labeled 25K in Table 1 of EMT04, where the rate is that according to Kunz et al. (2002), that the mass fraction of carbon at the center is $X(^{12}\text{C})=0.280$ (Table 4 of EMT04) at the end of core He-burning. In the case 25N, where the NACRE rate was adopted, $X(^{12}\text{C})=0.236$. In case 25C, where we have used the rate by Caughlan & Fowler (1988, hereafter CF88), $X(^{12}\text{C})=0.257$. Finally, the case labeled 25NM, where mass loss has been neglected during the evolution, has the lowest value $X(^{12}\text{C})=0.193$. This relatively reduced value is due to the higher central temperature achieved during core helium burning (see EMT04 for more details).

The lifetime of the core carbon burning phase in Table 3 of EMT04 is larger for a larger value of $X(^{12}\text{C})$ as is the mass of the convective core (indicated by M_{cc} in Table 3 of EMT04). In addition, §4 shows that shell carbon-burning is sensitive to the physical conditions achieved during core carbon-burning. In particular, it occurs in different regions of the star as indicated by Figures 4 to 10 of EMT04. A more detailed discussion of the effect of $X(^{12}\text{C})$ is available in EMT04. In the present work, we investigate its effect on the s-process itself. Our results are presented in §3 and §4.

4. In our previous calculation of the s-process (TEM00), we adopted a rate for the neutron-capture reaction $^{16}\text{O}(n, \gamma)^{17}\text{O}$ based on a cross section $\sigma_{16} = 0.20 \mu\text{b}$ according to Beer et al. (1992). However, in our present calculations, we have used the new rate for this reaction as obtained by Igashira et al. (1995). These authors have included the 434 keV resonance and obtained a cross section $\sigma_{16} = 34 \mu\text{b}$ at $T=30$ keV or 170 times larger than the cross section obtained by Beer et al. (1992). The new rate is given by:

$$\langle \sigma \rangle_{16} = (kT)^{-1/2} + 5.88(kT)^{1/2} \quad (1)$$

Since ^{16}O is a neutron sink, the new rate is expected to reduce the efficiency of the s-process during core He-burning, as has been emphasized by Rayet & Hashimoto (2000). Our results agree with this conclusion and are described in §3.

5. Another difference with our previous work (TEM00) on the s-process concerns the reactions $^{22}\text{Ne}(\alpha, n)^{25}\text{Mg}$ and $^{22}\text{Ne}(\alpha, \gamma)^{26}\text{Mg}$. The first reaction is known to be the main neutron source of the s-process in massive stars, while the second is a competing reaction since it captures part of the alpha particles.

Figure 1 illustrates the rate of the $^{22}\text{Ne}(\alpha, n)^{25}\text{Mg}$ reaction, where the NACRE rate is lower than that obtained by CF88 in the temperatures range below $T_8 \simeq 2.4$, a regime that comprises most of the core He-burning phase in the stars under consideration.

However, the NACRE rate is larger by a factor of up to three in the temperature range $T_8 \simeq (3 - 6)$, which is relevant to the more advanced burning phases, in particular the core and the shell carbon-burning. Fig. 1 displays the rate according to Jaeger et al. (2001), which shows some characteristics similar to the NACRE rate, although systematically slightly lower. Note that the situation at temperatures below $T_8 \sim 2.0$ is controversial. Fortunately this temperature range does not affect our results of the s-process. In §3, we show that the s-process yields do strongly depend on the value of the $^{22}\text{Ne}(\alpha, n)^{25}\text{Mg}$ reaction rate.

In our evolutionary calculations (EMT04), we have made a special effort to analyze the effects of several important physical quantities on the internal structure of the stellar models. Besides considering the variation in $^{12}\text{C}(\alpha, \gamma)^{16}\text{O}$ as described above, we have investigated the effects of mass loss on the structure of the stellar models.

Mass loss is certainly important for stars more massive than $15 M_\odot$, especially if the star evolves on the Kelvin-Helmholtz time scale to the red giant stage, where mass loss is known to increase significantly (de Jager et al. 1988). As shown in our previous paper (EMT04), a rapid evolution to the red giant branch occurs when the effect of the gradient of molecular weight is taken into account. In this case, the Ledoux criterion for convection inhibits the convective instability in the region of the hydrogen-burning shell. Such evolution is found in the calculation by Woosley et al. (2002) for the 15 and 25 M_\odot stars. We find that mass loss has an insignificant effect on the s-process during core He-burning. However, as we shall see in §4, the characteristics of shell-carbon burning are influenced, which may affect the s-process in turn.

3. s-Process in Core He-Burning: updated results

It is worth updating our previous results (TEM00) of the s-process during core helium burning in massive stars, mainly because many reaction rates determining the s-process efficiency have been revised as described in §2.

Table 2 presents a comparison of some key physical quantities characterizing the efficiency of the s-process during core He-burning for the stars indicated. Comparing our new results with the former ones, labeled TEM00 in Table 2, we see that the new results show a significantly reduced s-process efficiency. In particular, we obtain in the case of the 25 M_\odot star (case 25C) an overproduction factor of 618 for ^{80}Kr compared to 1100 in our former calculations (TEM00). This remarkable decrease by a factor of 1.8 is mainly due to the larger rate of $^{16}\text{O}(n, \gamma)^{17}\text{O}$ used in the present study. Both the present calculation (25C)

and that in TEM00 used the same rate for the $^{22}\text{Ne}(\alpha, n)^{25}\text{Mg}$ reaction. Therefore neutron capture on ^{16}O is an efficient sink of neutrons, especially during the advanced stage of core He-burning. It is interesting to note that Rayet & Hashimoto (2000) found a reduction of 1.2 to 1.6 due to this neutron sink. Hence, the statement in our previous work (TEM00) that most of the neutrons captured by ^{16}O will be returned by the reaction $^{17}\text{O}(\alpha, n)^{20}\text{Ne}$ is not fully justified because it was based on one-zone calculations in which the effect of convection was neglected.

In Tables 2 and 3 we show the effect of the lower NACRE rate for the $^{22}\text{Ne}(\alpha, n)^{25}\text{Mg}$ reaction (see Fig. 1) as compared with that due to CF88 in the temperature range up to $T_8 \simeq 2.4$. It is clear that the NACRE rate leads to a significantly reduced s-process efficiency: for example, Table 2 shows that the overproduction of ^{80}Kr in the case of the $25 M_\odot$ star is 174 with the NACRE rate while it is 618 with the rate of CF88, a reduction by a factor of 3.6. The low overproduction value is rather close to that obtained by Rayet & Hashimoto (2000). In their calculations for an $8 M_\odot$ helium star (corresponding roughly to an initial mass of $25 M_\odot$), they used the same rate as we do for $^{16}\text{O}(n, \gamma)^{17}\text{O}$ and considered different rates for $^{12}\text{C}(\alpha, \gamma)^{16}\text{O}$. They used the rate given by Drotleff et al. (1993) for the $^{22}\text{Ne}(\alpha, n)^{25}\text{Mg}$, which is quite similar to the NACRE rate shown in Fig. 1. Taking the “adopted” NACRE rate for $^{12}\text{C}(\alpha, \gamma)^{16}\text{O}$ (1.92 times larger than that of CF88 at $T_9=0.3$), they found an overproduction factor of 92 for ^{80}Kr . However, when they used the lower limit on the NACRE rate for $^{12}\text{C}(\alpha, \gamma)^{16}\text{O}$ ($1.16\times$ of CF88) the overproduction factor increased to 180. The difference between their results and our 25N model demonstrates the importance of the $^{22}\text{Ne}(\alpha, n)^{25}\text{Mg}$ rate. Our results in Table 2 may be considered an update of the results of Rayet & Hashimoto (2000), since our rate for the $^{12}\text{C}(\alpha, \gamma)^{16}\text{O}$ is based on a new compilation as described in §2.

One conclusion we may draw from the discussion above is that the efficiency of the s-process during core He-burning in massive stars depends crucially on the neutron production reaction $^{22}\text{Ne}(\alpha, n)^{25}\text{Mg}$ and on the neutron-sink reaction $^{16}\text{O}(n, \gamma)^{17}\text{O}$. Both reactions become effective during the late stage of core He-burning where the ^{16}O becomes abundant. Fortunately, the present uncertainty in the $^{12}\text{C}(\alpha, \gamma)^{16}\text{O}$ does not have a significant effect on the s-process efficiency, as indicated by the comparison of the results of the two cases “present work, NACRE” and “present work, (25K)” in which the rate for this reaction is different as described in §2. Table 2 show that the efficiency of the s-process is remarkably reduced for all the masses considered.

It is worth analyzing our results of the s-process when the NACRE rate is applied for the $^{22}\text{Ne}(\alpha, n)^{25}\text{Mg}$ reaction instead of using the CF88 rate. Fig. 2 displays several physical quantities as a function of the central helium mass fraction as obtained for the $25 M_\odot$

models 25N and 25C during core He-burning. The larger rate by CF88 leads to an increase in the neutron density (see Fig. 2b) at larger helium mass fraction (or at earlier time). Consequently, a higher neutron exposure, $\tau_n(m_r) \equiv \int_0^t n_n(m_r, t') v_{\text{th}} dt'$ (Clayton et al. 1961, Fig. 2c) is achieved leading to an earlier increase of the overproduction of ^{80}Kr (Fig. 2d). In other words, despite the higher peak neutron density achieved in case of the NACRE rate, the s-process is less robust because the neutron exposure is lower due to the shorter time scale until the end core He-burning. The conclusion of this discussion is that the s-process during He-burning in massive stars is a race against time since the whole process occurs during the late stage of this phase.

In Fig. 3 we present the overabundances of heavy nuclei averaged over the convective helium burning core for models 15N, 20N, 25N, and 30N, and in Tables 3 and 4 we list the overabundances of selected nuclei at the end of the core helium burning. The figures show that the larger the stellar mass, the more efficient is the neutron-capture of the s-process. The figures also show the well-known feature of the weak s-process that the overabundance distribution in the mass range $A = 60 - 90$ has a peak at ^{80}Kr .

4. s-process in shell carbon-burning

At the end of core helium burning, the star begins to contract, and, when its central temperature exceeds $\sim 5 \times 10^8$ K, the neutrino energy loss dominates the energy balance (Woosley et al. 2002). The carbon burning with its $^{12}\text{C} + ^{12}\text{C}$ reaction starts to be effective at temperature $\sim 6 \times 10^8$ K and density $\sim 3 \times 10^4$ g cm $^{-3}$ (EMT04). There are three effective reaction channels of $^{12}\text{C} + ^{12}\text{C}$ fusion and overall carbon burning converts most of the initial carbon primarily into ^{16}O , ^{20}Ne , ^{23}Na , $^{24,25,26}\text{Mg}$, ^{28}Si , and, secondarily, into ^{27}Al and $^{29,30}\text{Si}$ (Clayton 1983; Woosley et al. 2002).

In our previous evolution calculations (EMT04), we found that the carbon shell burning depends sensitively on the profile of ^{12}C resulting at the end of core carbon burning (Woosley et al. 2002; Imbriani et al. 2001; Arnett 1996). This profile depends in turn on how core carbon burning proceeds: in a convective core or in a radiative region. The nature of that burning depends on the central mass fraction of ^{12}C attained at the end of core helium burning, which is crucially influenced by the still uncertain $^{12}\text{C}(\alpha, \gamma)^{16}\text{O}$ reaction. Thus, the rate for $^{12}\text{C}(\alpha, \gamma)^{16}\text{O}$ has a significant influence on the behavior of the shell C-burning, as we have previously shown (EMT04). Our results of the s-process presented in the following are expected to depend on this rate as well.

The neutron source of the s-process nucleosynthesis during shell carbon burning is the

$^{22}\text{Ne}(\alpha, n)^{25}\text{Mg}$ reaction with an initial amount of $X(^{22}\text{Ne}) \simeq 10^{-2}$, the amount left over from the end of core helium burning. The alpha particles for the $^{22}\text{Ne}(\alpha, n)^{25}\text{Mg}$ reaction are the product of the $^{12}\text{C} + ^{12}\text{C} \rightarrow ^{20}\text{Ne} + \alpha$ reaction channel. The $^{22}\text{Ne}(\alpha, n)^{25}\text{Mg}$ cross section increases by a factor of $\sim 10^{10}$ from the phase of core helium burning ($T_9 \simeq 0.3$) to the phase of shell carbon burning ($T_9 \simeq 1.0-1.1$). The ^{22}Ne (^4He) mass fraction during the s-process of core helium burning is $\sim 10^{-1}$ ($\sim 10^{-2}$), whereas during the s-process of shell carbon burning, $X(^{22}\text{Ne}) \sim 10^{-2}$ ($X(^4\text{He}) \sim 10^{-9}$). These factors, together with the change in the density from $\sim 10^3 \text{ g cm}^{-3}$ during core helium burning to $\sim 10^5 \text{ g cm}^{-3}$ during shell carbon burning, explain the difference in the neutron density during the s-process of core helium burning ($n_n \sim 10^7 \text{ cm}^{-3}$) and the s-process of shell carbon burning ($n_n \sim 10^{10} \text{ cm}^{-3}$).

The consequence of the higher neutron density in the shell carbon burning is the opening of the (n, γ) path of some branchings in the s-process path. Particularly important in the weak s-process are the branchings at ^{79}Se and ^{85}Kr . To illustrate the consequence, we take the data of ^{79}Se at $T=26 \text{ keV}$, $\langle \sigma_{n, \gamma} \rangle = 225 \text{ mb}$ and beta-decay $t_{1/2} = 5.46 \text{ yr}$ and at $T=91 \text{ keV}$, $\langle \sigma_{n, \gamma} \rangle = 97.3 \text{ mb}$ and beta-decay $t_{1/2} = 0.38 \text{ yr}$ (Raiteri et al. 1993). The time scale of beta-decay is $\tau_\beta = t_{1/2}/\ln(2)$ and the time scale of neutron capture is $\tau_n = 1/n_n \langle \sigma v_{th} \rangle$, where the neutron thermal velocity $v_{th} = 2.4 \times 10^8 (T/30 \text{ keV})^{1/2} \text{ cm s}^{-1}$. Therefore when $\tau_\beta = \tau_n = \tau$, at $T=26 \text{ keV}$, $n_n = 8.0 \times 10^7 \text{ cm}^{-3}$ and at $T=91 \text{ keV}$, $n_n = 1.4 \times 10^9 \text{ cm}^{-3}$. This implies that during core helium ($T \simeq 26 \text{ keV}$) with $n_n \simeq 10^7 \text{ cm}^{-3}$ ($< 8.0 \times 10^7 \text{ cm}^{-3}$) most of ^{79}Se beta-decays to $^{79}\text{Br}(n, \gamma)^{80}\text{Br}(\beta^-)^{80}\text{Kr}$, producing ^{80}Kr . However, during shell carbon burning ($T \simeq 91 \text{ keV}$), with $n_n \simeq 10^{10} \text{ cm}^{-3}$ ($> 1.4 \times 10^9 \text{ cm}^{-3}$), the path of neutron capture $^{79}\text{Se}(n, \gamma)$ is available and less ^{80}Kr is produced. The path differences followed by the s-process during these two burning phases produce different ratios of ^{80}Kr and ^{82}Kr abundances.

4.1. Shell Carbon Burning and Its s-process Characteristics

Figures 4 to 10 of EMT04 show the convective structure of our stellar models. Particularly relevant for this section are the various locations of the carbon convective shells. In Table 5 we present some of the properties of the last shell carbon burning phase in our stellar models. In Figure 4 we show the overabundance factors of heavy nuclei averaged over the convective carbon burning shell for model 15N, 20N, 25N, and 30N, and in Tables 3 and 4 we tabulate some of their values. The nucleosynthesis products from this carbon shell are the parts of the carbon shells that would be ejected in the supernova event. The locations, the mass ranges, and the durations of the C-shell burning are not well correlated from one stellar model to the others perhaps because of the variations due to the mass fraction of ^{12}C .

produced at the end of core helium burning, to the temperature and density variations with the stellar mass, and to the neutrino energy loss. However, although the temperature and density of the innermost region of the carbon burning shell vary quite significantly during the convective carbon burning, their average values are quite similar among the models. The average temperature at the bottom of convective shell is $\sim 1.0\text{-}1.1 \times 10^9 \text{K}$ and the average density is $\sim 1\text{-}2 \times 10^5 \text{ gm cm}^{-3}$.

The change of neutron exposures during shell C burning $\Delta\tau_n$ at the bottom of the C-shell convective zones (shown in Table 5) is significantly lower than the central τ_n produced at the center during core helium burning (shown in Table 2) by at least a factor of $4\times$. The average neutron exposures over convective zones $\langle\tau_n\rangle$ produced during C-shell burning are also lower than during core helium burning by a factor of 2 in the $15 M_\odot$ model and by a factor of 7 in the $30 M_\odot$ model. The ratio of the average neutron capture per iron seed over the convective regions $\langle\Delta n_c\rangle$ of core helium burning (Table 2) relative to the value produced by carbon shell (Table 5) is ~ 1 for the $15 M_\odot$ model, increases to ~ 2 for the $20 M_\odot$ model, and to $\sim 4\text{-}7$ for the $25 M_\odot$ models, and to ~ 7 for the $30 M_\odot$ model. This shows the trend of increasing robustness of the s-process in the carbon shell with decreasing stellar mass.

The maximum neutron density n_n^{max} at the bottom of the convective C-shell varies from $1.0 \times 10^{10} \text{ cm}^{-3}$ to $70 \times 10^{10} \text{ cm}^{-3}$ among our models, as shown in Table 5. The large variation is due to the fact that the $^{22}\text{Ne}(\alpha, n)^{25}\text{Mg}$ rate varies by a factor of $17\times$ for a 15% change of temperature near $T=1 \times 10^9 \text{K}$. The difference in temperatures and densities at the bottom of the convective C-shell among models is about $\sim 20\%$. These physical variables also vary during the C-shell evolution as a result of the C-shell burning itself or of the inner Ne and O shell burning. Interestingly, the higher the temperature and density of the C-shell, the shorter the burning duration. This results in roughly the same neutron exposure despite the higher neutron density.

The shell carbon burning decreases the mass fraction of ^{22}Ne by at least a factor of 5 from the value of $X(^4\text{He}) \simeq 10^{-2}$ at the end of core helium burning to $X(^4\text{He}) \simeq 10^{-3}$ at the end of shell carbon burning. This low value of $X(^{22}\text{Ne})$ near the end of core oxygen burning prevents significant change to the heavy element abundances during the short time left before the star explodes. During the explosive phase, little subsequent alteration occurs except for zones that achieve temperatures in excess of $T_9 \approx 2.3$. In such zones, the rate of $^{22}\text{Ne}(\alpha, n)^{25}\text{Mg}$ increases by a factor of 3×10^4 relative to the rate at $T_9=1.0$, but the dynamic time scale decreases by a factor of 10^7 relative to the time scale during shell carbon burning. Only disintegration reactions are likely to modify the abundances in these zones significantly during the explosion (e.g., Arnould & Goriely 2003).

The overabundance of ^{88}Sr increases by a factor of ~ 2 during shell carbon burning in

each model studied, and these overabundances increase monotonically with increasing stellar mass. In contrast to this, the overabundances of ^{80}Kr decrease during shell carbon burning for sequences 25N, 25NM, and 30N. In these sequences, a significant fraction of the convective carbon shell has a neutron density larger than $\sim 1.2 \times 10^9 \text{ n cm}^{-3}$. At this neutron density (and at a temperature $T \approx 30 \text{ keV}$), the neutron-capture rate of ^{79}Se dominates its beta-decay rate. This allows the s-process flow to bypass ^{80}Kr thereby leading to its destruction (see also Raiteri et al. 1991a). We show this in more detail in the next section.

4.2. $25 M_{\odot}$ s-process abundances

In this section, we describe how the abundances of the s-process products change with time as a massive star evolves through core He-burning and through shell C-burning. We focus on the products of the s-process in the last shell C-burning because these layers will be ejected mostly without further nucleosynthesis processing in a supernova explosion.

In Fig. 5 overabundance factors are shown as a function of time for the important nuclear species produced by the s-process during core He-burning and shell C-burning in a $25 M_{\odot}$ star (evolutionary sequence labeled 25N in Table 1). These curves represent the overabundance factors at a mass coordinate $M_r = 2.26 M_{\odot}$, that is, at a mass shell inside the convective core during core helium burning but at the bottom of the convective carbon-burning shell in this case (see Fig. 6 in EMT04). The overabundances of all nuclear species shown in Fig. 5 increase during core He-burning except $^{54,56}\text{Fe}$, ^{70}Zn , and ^{152}Gd , which decrease because of neutron capture. As expected, the pure s-nuclei (^{70}Ge , ^{76}Se , ^{80}Kr , ^{82}Kr , ^{86}Sr , ^{87}Sr) are produced in particular during this phase, as summarized in Table 3.

The modification of the s-process products by shell C-burning is most effective during core neon burning and core oxygen burning in case 25N, as shown in Fig. 5 at the time coordinate between 0.0 and -1.0. In this case, the convective carbon-burning shell is most effective as it has settled in the mass range $2.26\text{-}4.94 M_{\odot}$ (see Table 5 and Fig. 13). Note that the increase of the overabundance of ^{87}Rb before the onset of shell C-burning is a result of the β^+ -decay of ^{87}Sr , whose rate is sensitive to temperature according to the work of Takahashi & Yokoi (1987).

Figs. 5, 6, and 7 show that the effect of shell C-burning on the overabundance factors is distinct from that due to core He-burning (time coordinate between 4.0 and 5.0) for case 25N, 25K, and 25C, respectively. The neutron density achieved in case 25 N during shell C burning achieves a peak value of $\simeq 7 \times 10^{11} \text{ cm}^{-3}$ (see Fig. 8). Therefore, the branchings at the sites of the unstable nuclei ^{63}Ni , ^{69}Zn , ^{79}Se , and ^{85}Kr become effective. This can be

traced in Fig. 5 and Table 3 as follows:

- The decrease of the overabundance of ^{63}Cu and ^{65}Cu and the increase of ^{64}Ni indicate the branching at ^{63}Ni .
- The branching at ^{69}Zn is indicated by the increase of the overabundance of ^{70}Zn and the decrease of the abundance ratio of the Germanium isotopes $^{70}\text{Ge}/^{72}\text{Ge}$. Notice that ^{70}Zn was destroyed during core He-burning, but produced by shell C-burning (see 4.2.1 for more discussion on ^{70}Zn).
- The branching at ^{79}Se leads to a modification of the overabundance of the isotopes $^{80,82}\text{Kr}$. However, the overabundance of ^{80}Kr is diminished by a factor of about 4 compared to its value reached at the end of core He-burning while the overabundance of ^{82}Kr increases by a factor of about 1.7.
- The effect of the branching at ^{85}Kr leads to the increase of the overabundance of the isotopes ^{87}Rb (Raiteri et al. 1993).
- Finally, there is a decrease in the abundance of the isotopes $^{86,87}\text{Sr}$ (affected by the branchings at ^{85}Kr and ^{86}Rb) and an increase of the overabundance of ^{96}Zr to a value larger than 1 (^{96}Zr is destroyed during core helium burning).

In the cases 25K, the second stage of convective shell carbon-burning comprises an extended mass range of 1.30-4.54 M_{\odot} (see Table 5). The overabundance factors are shown in Fig. 6 and are taken at a mass coordinate of 1.38 M_{\odot} specifying the bottom of the convective carbon-burning shell in this case with its physical condition as a function of time shown in Fig. 9. These factors are distinct from those in the case 25N in many respects:

- The overabundance of ^{80}Kr is increased by shell C-burning in contrast to the case in 25N. The reason is the lower neutron density achieved during this phase in this sequence (see Fig. 9).
- This lower neutron density explains the lower overabundance factor of ^{86}Kr (about a factor 5 lower than in case 25N) and also the relatively higher overabundance of $^{86,87}\text{Sr}$. In other words, the nuclear-reaction flow in case 25K does not proceed beyond the Sr isotopes to reach the Zirconium region, as in case of 25N.

In the case of 25C the overabundance factors are displayed in Fig. 7. Despite the similarity with Fig. 6, the s-process is generally more efficient in this sequence in both the core He-burning or the shell C-burning due to the adoption of the CF88 rates.

It is worth relating these differences to the evolution of the stellar models. To do so, we compare Figures 8 and 9, which show several physical variables characterizing the properties of the carbon-burning shell in the cases 25N and 25K, respectively. We recall that 25N at the end of core helium burning has a central carbon mass fraction $X(^{12}\text{C})=0.236$ while the 25K has $X(^{12}\text{C})=0.280$. This slight difference has a significant effect on the ensuing evolution beyond core He-burning, as described in detail by EMT04.

We emphasize some points that help to understand the s-process during shell C-burning. The shell burning proceeds differently in the sequence 25N and 25K. The relatively lower value of $X(^{12}\text{C})$ of the sequence 25N leads to a convective core of mass $M_{CC}=0.36 M_{\odot}$, while $M_{CC}=0.47 M_{\odot}$ in the case 25K. Due to this difference, shell C-burning proceeds in 25N in three convective episodes but in two convective episodes in 25K. This can be seen in Figs. 8 and 9, especially in the behaviour of the neutron number density as a function of time. A peak value of the neutron density of $\sim 7 \times 10^{11} \text{ cm}^{-3}$ is achieved in 25N compared to $\sim 1.1 \times 10^{10} \text{ cm}^{-3}$ in case 25K. The higher neutron density in 25N creates a flow of neutron-capture reactions which reaches the region of Zirconium (see Fig. 12). On the other hand, the third convective C-shell phase in 25N lasts ~ 0.5 yr, while the second convective C-shell in 25K lasts for ~ 24 yr, or $\sim 50 \times$ longer. This longer burning time leads to more depletion of carbon in the C-shells where $X_f(^{12}\text{C})=7.2 \times 10^{-3}$ in 25K compared to $X_f(^{12}\text{C})=9.4 \times 10^{-2}$ in 25N.

The neutron density and the duration of neutron exposure in the two models produce the neutron exposure, $\tau_n \simeq 0.9 \text{ mbarn}^{-1}$ at the bottom of the respective convective carbon shells. However, the longer duration and larger mass range of convective carbon shell burning in 25K ($M_r = 1.30\text{-}4.54 M_{\odot}$) than in 25N produces a higher value of neutron capture per iron seed nucleus n_{cap} in 25K (see Figs. 8 and 9). In order to explain those values of τ_n and n_{cap} , we performed several test calculations of nuclear burning and mixing of the convective zones.

As a reference calculation, we constructed spherical shells with the temperatures, densities, diffusion coefficients, and mass coordinates of model 25K when the convective C-shell is at its maximum extent ($M_r = 1.30\text{-}4.54 M_{\odot}$). As the initial composition of all test calculations of C-shell burning, we took the composition of the stellar model at the end of core helium burning, at which point $n_{cap}=3.70$. We ran a simultaneous nuclear burning and mixing code (Jordan et al. 2005) for about 20 yrs duration so that $X_f(^{12}\text{C}) \leq 1 \times 10^{-3}$. In this simultaneous burning and mixing code, the temperature, density, and diffusion coefficient of each zone remained fixed in time for simplicity. The results of this reference calculation show a neutron exposure at the bottom of the convective shell of $\tau_n=0.20 \text{ mbarn}^{-1}$ and a number of neutrons captured per Fe seed of $n_{cap}=4.74$.

To understand the effect of the size of convective zones (since model 25N has a thinner range of convective zones than in model 25K), we ran a second calculation in which we reduced the thickness of convective zones to about 70% in mass range. We kept the other variables the same as in the reference calculation. In this second calculation, we obtained $\tau_n=0.07 \text{ mbarn}^{-1}$ and $n_{cap}=4.74$ by the time $X_f(^{12}\text{C})$ had dropped to 1×10^{-3} in about 20 years. This shows that the less available neutron source due to the reduced size of convective zones produces a smaller value of neutron exposure. On the other hand, there were a correspondingly smaller number of seed nuclei, so the number of neutron captures per Fe seed nuclei was the same as in the reference calculation. The relation between this test calculation to the reference one clearly does not mimic the relation between the 25N and 25K results.

To test the effect of the higher temperature in the carbon shell in 25N, we performed another test calculation in which we kept all physical variables the same as in the reference calculation but increased the temperature of each zone by 15%. For this structure, we found $\tau_n=0.21 \text{ mbarn}^{-1}$ and $n_{cap}=3.85$ at time $t=0.04 \text{ yr}$ and $\tau_n=0.26 \text{ mbarn}^{-1}$ and $n_{cap}=4.86$ at time $t=20 \text{ yr}$. This test shows that the structure with higher temperature produces a much higher neutron density and hence the same value of τ_n ($\approx 0.2 \text{ mbarn}^{-1}$) as in the reference calculation but in only 0.04 years. Because of the shorter time to reach $\tau_n = 0.21 \text{ mbarn}^{-1}$, this test calculation yields a smaller value of n_{cap} at the same τ_n . This result indeed mimics the difference between the results of 25N and 25K, and we conclude that the similar values of τ_n in the C-shell of 25N and 25K and the higher value of n_{cap} in 25K at the end of their C-shell burning is mostly due to the higher temperature in 25N than in 25K.

In Figure 10 we show the overabundance distribution of ^{12}C , ^{16}O , ^{22}Ne , ^{70}Zn , ^{70}Ge , ^{80}Kr , and ^{86}Sr -nuclei that are important for the s-process nucleosynthesis during shell carbon burning—at the end of core oxygen burning for sequences 25N and 25K to illustrate Table 3 and the discussion above. The values of the overabundances of light nuclei ^{12}C , ^{16}O , and ^{22}Ne drop significantly from 92(78), 72(77), 60(59) at the end of core helium burning to 2.4(31), 61(68), and 3(5) at the end of core oxygen burning for the last carbon shell region in sequence 25K(25N), respectively. The overabundance of the s-only nuclide ^{70}Ge increases by a factor of $\sim 2\times$ for both sequences during shell carbon burning. The overabundance of ^{70}Zn at the end of core helium burning is 0.4 for sequences 25N and 25K, but increases significantly to a value of 5 for sequence 25K and to a value of 40 for sequence 25N during shell carbon burning, as shown in the figure.

Our general conclusion of this analysis is that s-process nucleosynthesis occurring in shell C-burning is rather sensitive to the central mass fraction of ^{12}C attained at the end of core He-burning, and this in turn depends on the rate of $^{12}\text{C}(\alpha, \gamma)^{16}\text{O}$, a value still under

debate, as outlined in §2.

4.2.1. ^{70}Zn

The production of ^{70}Zn in explosive carbon and neon burning is discussed in Arnett (1996). The source of neutrons for the neutron-capture reactions in explosive burning is the $^{12}\text{C}+^{12}\text{C}$ reaction. In C or Ne explosive burning, ^{70}Zn is produced in almost equal amounts as ^{68}Zn (Arnett 1996; Howard et al. 1972) whereas the ratio of ^{70}Zn to ^{68}Zn in solar abundance is 0.033. An analysis by Arnett (1996) concludes that solar ^{70}Zn is produced in a nuclear burning process with time scale that is longer than a typical explosive time scale, which suggests the hydrostatic burning of carbon or neon as the site production of ^{70}Zn . In such burning, the ^{70}Zn overproduction should be a fraction of ^{68}Zn overproduction, as we find in the present analysis.

The solar abundance of ^{70}Zn isotope is 0.62% of all Zinc isotopes (Anders & Grevesse 1989). The small fraction of ^{70}Zn abundance relative to other Zinc isotopes makes it difficult to detect in the spectra of stellar atmosphere or interstellar medium. It is possible that hints of ^{70}Zn might be preserved in meteoritic samples. For example, ^{70}Zn isotopic anomalies have been measured in Allende meteorite inclusions. A clear excess of ^{66}Zn and a deficit of ^{70}Zn in FUN inclusions (Volkening & Papanastassiou 1990; Loss & Lugmair 1990) is correlated with excesses for the neutron-rich isotopes of ^{48}Ca , ^{50}Ti , ^{54}Cr , and ^{58}Fe . The source of these anomalies was attributed to neutron-rich e-process nucleosynthesis in massive stars (Hartmann et al. 1985), but the current thinking is that these isotopes were produced in rare Type Ia supernova (e.g., Meyer et al. 1996; Woosley 1997). Since such nucleosynthesis does not produce ^{70}Zn , the correlated deficit of this isotope with excesses in ^{48}Ca , for example, is expected. A more promising cosmochemical sample that might provide evidence of ^{70}Zn production in C-shell s-processing is a presolar grain. It is quite reasonable to expect that some shell carbon burning products might condense or be implanted into grains which, if then preserved in meteorites, would show the excesses of ^{70}Zn and ^{87}Rb isotopes, along with other s-process products listed in Table 3 for correlation analysis.

4.2.2. ^{87}Rb

Rb solar abundance is comprised of ^{85}Rb and ^{87}Rb isotopes with the ^{87}Rb abundance 27.8% of the total (Anders & Grevesse 1989). The abundance of the long-lived radioactive ^{87}Rb , which decays to daughter nuclei ^{87}Sr with a half-life of 4.9×10^9 yr, is often used

in radioactive dating of rocks and meteorites (e.g., Cowley 1995; Misawa et al. 2006). It is probably not possible to observe Rb isotope ratio directly from massive stars, however, the ejected abundances into interstellar medium or molecular clouds could be measured. Recently Federman et al. (2004) reported the first measurement of the interstellar $^{85}\text{Rb}/^{87}\text{Rb}$ isotope ratio from the diffuse gas toward ρ Oph A. They obtained a value of 1.21 which is significantly lower than the solar abundance value of 2.59. A proper understanding of the origin of ^{87}Rb in the diffuse gas will require chemical evolution calculations with mixing of several generations of stars. Correlating the ^{87}Rb observed abundance with other heavy isotopic abundances could reveal interesting insights into carbon-shell nucleosynthesis.

4.3. s-process path

In order to see the differences in the s-process paths of core helium burning and shell carbon burning, we performed two one-zone s-process nucleosynthesis calculations using the central temperature, central density, central mass fraction $X(^4\text{He})$ of the core helium burning in sequence 25N and the temperature, density, and mass fraction $X(^{12}\text{C})$ of the innermost shell of the shell carbon burning in sequence 25N, respectively. The initial composition of the calculation is taken from the initial composition of the burning phase in sequence 25N. For each time step, we compute the reaction flow. For example, for the reaction $i + j \rightarrow k + l$, the integrated flow over time step dt is $f_{i+j,k+l} = N_A \langle \sigma v \rangle_{ij,kl} \rho Y_i Y_j dt$, where Y_i and Y_j are the abundances of species i and j , respectively. The total of the integrated net flow for all timesteps, $F_{i+j,k+l} = \sum_n [f_{i+j,k+l} - f_{k+l,i+j}] dt_n$ shows the total flow of the reaction. The net integrated nuclear reaction flows are shown for the case 25N in Fig. 11 and Fig. 12 for the s-process during core He-burning and shell C-burning, respectively. Similar features shown in Fig. 11 and Fig. 12 are also reproduced in sequence 25K. The differences in temperature, density, and, therefore, the neutron density, cause some differences in the branchings of the flows. The (n,γ) branching paths that are opened or enhanced during the third convective C-shell relative to s-process paths during the core helium burning in 25N are at $^{57,60}\text{Fe}$, ^{64}Cu , ^{69}Zn , ^{70}Ga , ^{75}Ge , ^{76}As , ^{81}Se , $^{80,82}\text{Br}$, ^{85}Kr , $^{86,87}\text{Rb}$, $^{87,89,90}\text{Sr}$, ^{90}Y , and ^{95}Zr .

It is interesting to note that Fig. 12 shows that proton-capture reactions occur on nuclei with $Z=26-30$ during shell C-burning. The largest (p,γ) flow for $Z \geq 26$ is the $^{58}\text{Fe}(p,\gamma)$ flow. The ratio of $^{58}\text{Fe}(p,\gamma)/^{58}\text{Fe}(n,\gamma) \simeq 1.4 \times 10^{-3}$, which clearly shows that proton capture reactions do not affect the s-process flow.

In these one-zone nucleosynthesis calculations of shell carbon burning, we find the five largest neutron source reactions are the (α,n) reactions on ^{22}Ne , ^{21}Ne , ^{17}O , ^{13}C , and ^{26}Mg , with ^{21}Ne produced through $^{20}\text{Ne}(n,\gamma)^{21}\text{Ne}$, ^{17}O produced through $^{16}\text{O}(n,\gamma)^{17}\text{O}$, ^{13}C pro-

duced through $^{12}\text{C}(\text{p,g})^{13}\text{N}(\beta^+)^{13}\text{C}$, and ^{26}Mg produced through $^{12}\text{C} + ^{12}\text{C} \rightarrow ^{23}\text{Na} + \text{p}$ followed by $^{23}\text{Na}(\alpha,\text{p})^{26}\text{Mg}$. The alphas (58%) and protons (42%) are produced by the two channels of carbon burning.

Recently Travaglio et al. (2004) in their study of Sr, Y, and Zr Galactic evolution infer some hints of a primary s-process in low-metallicity massive stars. These authors suggested that $^{12}\text{C} + ^{12}\text{C} \rightarrow ^{23}\text{Mg} + \text{n}$ and $^{26}\text{Mg}(\alpha,\text{n})^{29}\text{Si}$ during carbon burning could be the neutron source reactions in the extremely metal poor (EMP) massive stars. To analyze this suggestion, we evolved a $25 M_{\odot}$ star with initial metallicity $[\text{O}/\text{H}]=[\text{Fe}/\text{H}]=-4$ up to the end of core helium burning and then took this composition as the initial composition of a one-zone calculation of shell carbon burning using the physical conditions of sequence 25N above. We find the ratios of α , p, and n channels of $^{12}\text{C} + ^{12}\text{C}$ reaction flow are 1.0:0.71:0.0, respectively. The largest neutron source reactions are the (α,n) reactions on ^{13}C , ^{17}O , ^{21}Ne , and ^{22}Ne with their ratios of 1.0:0.17:0.06:0.02, respectively. The $^{13}\text{C}(\alpha,\text{n})^{16}\text{O}$ reaction is the major neutron source during shell carbon burning, which can also be shown for core helium burning (Baraffe et al. 1992; Rayet & Hashimoto 2000), instead of the $^{22}\text{Ne}(\alpha,\text{n})^{25}\text{Mg}$ reaction in the EMP massive star. We find that most of the Sr nuclei (77%) are produced in core helium burning rather than in the shell carbon burning. Therefore, carbon burning could not provide enough neutrons to explain the enhancement of the observed Sr abundances in the EMP stars.

5. Neutron Exposure and Neutron Capture per Iron Seed Nuclei

Several burning sequences in massive stars produce neutrons through the $^{22}\text{Ne}(\alpha,\text{n})^{25}\text{Mg}$ reaction. A simple way to show where nuclei are exposed to these neutrons during the stellar lifetime is to plot the total neutron exposure versus the interior mass radius as shown in Fig. 13 at the end of core oxygen burning (the last model calculated). $\tau_n(M_r) \equiv \int_0^t n_n(M_r, t') v_{\text{th}} dt'$, is the neutron exposure that would be experienced by a nucleus if it remained at M_r at all times (TEM00). No nucleus has this history because of convective mixing in the star, but Fig. 13 clearly shows where neutrons were liberated during the star's evolution.

The central neutron exposure of each curve in Fig. 13 is mostly due to the neutron exposure during core helium burning (TEM00). Farther out are several peaks of neutron exposures produced during shell carbon burning. As in the core helium burning, the highest neutron exposure occurs at the innermost convective region where the temperature and density are the highest and the neutron-liberating reactions the fastest. It is worth remembering that convection continually replenishes the supply of neutron sources to these zones.

The outermost peak of the neutron exposure curves in Fig. 13 are due to the shell helium burning. The width of the peak is due to the outward migration of the innermost part of the helium shell during its evolution.

While the neutron exposure as function of interior radius, $\tau_n(M_r)$ is a good tool to show where nuclei are exposed to neutrons, it is less effective in showing the degree of production of heavy nuclei. As mentioned above, convective mixing moves nuclei into and out of the regions of high neutron density, so no nucleus actually experiences an exposure $\tau_n(M_r)$. A direct measure of the global production of heavy elements is $N_c = \int n_c(M_r) dM_r$, the number of neutron captures per iron seed nucleus at different phases of the stellar evolution integrated over mass range above the mass cut, $1.5 M_\odot$ and within the relevant burning zone. $n_c(M_r)$ is the number of neutron captures per iron seed nuclei at interior radius M_r at the burning phase. In Table 7 we present N_c of our stellar models. That table shows that in each stellar model, the s-process during core helium burning is the dominant producer of ejected s-process heavy elements, followed by the s-process during carbon burning, and then the s-process during shell helium burning, except for the case of $15 M_\odot$ where the mass cut of $1.5 M_\odot$ is comparable to the maximum size of its convective helium burning core of $2.22 M_\odot$.

If we compare N_c of different the stellar masses in Table 7, we find that the larger the stellar mass, the greater the heavy element production in each s-process burning phase. It is interesting to note that our $30 M_\odot$ stellar model produces a larger total amount of heavy elements than the $25 M_\odot$ stellar model even after weighting by an initial mass function factor. We surmise that the largest weak s-process production is for stellar mass around $25 - 30 M_\odot$.

6. Comparison of Stellar Yields with Solar Abundance

Stellar nucleosynthesis yields can be tested with abundance measurements of interstellar medium, stellar atmosphere, presolar grains in meteorites, or solar system abundance. In this section, we compare our stellar yields with solar system abundance. In order to make a proper comparison with solar system abundances, a Galactic Chemical Evolution calculations where time-integrated yield contributions from multi generations of stars of different metallicities should be carried out (Busso et al. 1999). However, since we only produce a limited mass range of stellar models and only of initial solar metallicity, a meaningful comparison is done in a simplistic approach that we compare the s-only solar abundances with the sum of the IMF-averaged yields of the s-only nuclei of our stellar models and of the s-only nuclei contribution from the main component. We use the overproduction factors, X/X_\odot for the comparisons.

As the overproduction factors of the main component are the ratios of the values of the third and the second columns of Table 2 of Arlandini et al. (1999). Our approach is similar with the analysis performed by Arlandini et al. (1999) in decomposing the solar abundance distribution into the s- and r-process components. Arlandini et al. (1999) calculated the r-component residuals by subtracting the s abundances of the arithmetic average of their 1.5 and 3 M_{\odot} models at $Z = Z_{\odot}/2$ from the solar abundance. They showed in their Fig. 3 that with their new (n, γ) cross sections of neutron magic nuclei at $N=82$, the agreement between their low-mass asymptotic giant branch s-only nuclei yields and their corresponding solar abundances improved significantly.

The IMF-averaged overproduction factors of our stellar models, y_{wk} is calculated as $y_{wk} = [r_{12.5-17.5} \times y_{15} \times 13.5 + r_{17.5-22.5} \times y_{20} \times 18.5 + r_{22.5-27.5} \times y_{25} \times 23.5 + r_{27.5-40.0} \times y_{30} \times 28.5] / (r_{12.5-17.5} \times 13.5 + r_{17.5-22.5} \times 18.5 + r_{22.5-27.5} \times 23.5 + r_{27.5-40.0} \times 28.5)$ where we assume each stellar model ejects all its material into interstellar medium except for its 1.5 M_{\odot} remnant and only stars in the mass range of 12.5 M_{\odot} and 40 M_{\odot} eject weak s-process materials. y_{15} , y_{20} , y_{25} , and y_{30} are the stellar overproduction factors of our 15, 20, 25, and 30 M_{\odot} models (some are listed in Table 6). The factors $r_{12.5-17.5}$, $r_{17.5-22.5}$, $r_{22.5-27.5}$, and $r_{27.5-40.0}$ are the normalized-number of stars in the mass range of 12.5-17.5 M_{\odot} , 17.5-22.5 M_{\odot} , 22.5-27.5 M_{\odot} , and 27.5-40.0 M_{\odot} , respectively, assuming their ratios follow the IMF distribution $\xi_0 m^{-\alpha}$ with Salpeter’s original value $\alpha=1.35$.

Our weak s-only nuclei overproduction factors, y_{wk} , are scaled and summed with the scaled main s-only nuclei overproduction factors to produce the total s-only nuclei overproduction factors, y_{s-tot} such that: $y_{s-tot} = c_{wk} \times y_{wk} + c_{mn} \times y_{mn}$. The scale factors c_{wk} and c_{mn} are determined by least-square fit of the total s-only overproduction factors relative to the solar values of unity. We use the 34 s-only nuclei from ^{70}Ge up to ^{208}Pb in the fit. Their standard deviations are taken from column 4 of Table 2 of Arlandini et al. (1999) where the values were determined by taking into account the uncertainties in cross sections and solar abundances. The best fit of the total s-only nuclei overproduction factors is represented by the solid circles in Fig. 15. In this figure, the s-only overproduction factors of the weak component are from our stellar models (15N, 20N, 25N, and 30N) at the end of core oxygen burning and are represented by the filled diamond symbols, whereas the s-only overproduction factors of the main component are represented by the solid squares. The value of the best-fit χ^2 is 153.7 with 32 degrees of freedom. The value of the best-fit χ^2 is quite large suggesting that we may be underestimating the standard deviations (we have not taken into account the error propagation of the cross sections to the yields of our stellar models). Alternatively, the large χ^2 may be due to our too simple treatment of chemical evolution or the fact our stellar models began with initial solar composition. Nevertheless, we show that the fit of the s-only nuclei of the weak component ($A < 90$) is as good a fit as the fit of the

main component ($A > 90$). We expect that if the overproductions due to explosive burning and from the complete set of nuclei from the main components are included, most of the points on Fig. 15 would lie near the dashed line in the figure (solar values).

Table 8 presents the best fit overproduction factors of the weak and main components of the s-only nuclei, of nuclei in the mass range $60 < A < 90$ and overproduction factor >0.5 , and of some other interesting heavy nuclei. We find that our set of stellar models using NACRE reaction rates produces too many ^{70}Ge and ^{82}Kr nuclei, at maximum the excesses are 14% and 13%, respectively. For s-only nuclei with $A \leq 87$, the weak component contributes at least 40% of the solar s-only nuclei. For s-only nuclei with $A > 90$, most of the weak component contributions are between 5.3% and 8.5% except for ^{152}Gd , ^{187}Os , and ^{198}Hg which are 14%, 13%, and 11%, respectively.

In principle, the method presented in this section is similar to the classical approach of fitting σN_s curve solar abundance pioneered by Seeger et al. (1965) and Clayton & Rassbach (1967). Both methods fit the s-only nuclei of solar abundances. In the classical approach, seed nuclei are exposed with three exponential distributions of neutron exposures (the main, the weak, and the strong component), whereas in the stellar models seed nuclei are exposed with a single exposure in massive stars (Beer 1986; Beer & Macklin 1989) and an exponential exposure from repeated thermal pulses in the low-mass AGB stars (Ulrich 1973).

6.1. Comparison of s-process Burning Phase and Single Stellar Model

It is interesting to know how good the s-only nuclei overproduction factors of each stellar model at the end of core helium burning, at the end of core oxygen burning, and their IMF-averaged are relative to the best overall fit to the s-only solar abundance distribution. In Fig. 16 we present the best-fit overproduction factor distribution of model 30N at the end of core helium burning (panel a), of the IMF-averaged of our stellar models at the end of core helium burning (panel b), of model 25N at the end of core oxygen burning (to include s-process results from core helium and shell carbon burnings, panel c), and of the IMF-averaged of our stellar models at the end of core oxygen burning (panel d). In panel d, instead of model 25N for the $25 M_\odot$ contribution (shown in Fig. 15), we take model 25K for testing the effect of $^{12}\text{C}(\alpha,\gamma)^{16}\text{O}$ reaction in fitting the s-only solar abundance.

Model 30N (Fig. 16a) produces the best s-only solar distribution fit with $\chi^2=176$ among 15N, 20N, 25N, 25K, and 30N models for yields at the end of core helium burning. Model 30N also produces a better fit than the IMF-averaged of models at the end of core helium burning ($\chi^2=205$, Fig. 16b), mostly due to the large χ^2 contribution from the 15 and $20 M_\odot$

models.

Model 25K (Fig. 16c) produces the best fit to the s-only solar distribution with $\chi^2=161$ among 15N, 20N, 25N, 25K, and 30N models for yields at the end of core oxygen burning. We also find the overproduction of s-only nuclei of the IMF-averaged of models at the end of core oxygen burning ($\chi^2=153$) gives a better fit to the s-only solar distribution than the overproductions of the IMF-averaged of models at the end of core helium burning ($\chi^2=206$). The differences in χ^2 between the fits in the panels of Fig. 16 being larger than 8 are quite significant since the differences only involve 6 data points for the weak component. We conclude that including shell carbon burning s-processing indeed gives a better fit to the s-only solar distribution nuclei than using yields from the core helium burning s-process only. Also IMF-averaging is necessary to give a better fit to the solar abundance distribution (as can be seen by comparing the χ^2 and the spread from min to max of overproduction factors of panel c with the distribution of panel d). Furthermore, the overproduction factors $X/X_{\odot} > 0.5$ for nuclei with $60 \leq A \leq 90$ suggest that solar abundances of nuclei in this mass range are dominantly produced by the s-processing in massive stars (see also Table 8).

7. Summary and Discussion of the Results of the s-process

Tables 3, 4, and 6 summarize our results on the s-process in the massive stars under consideration. In Table 3, we emphasize the following points:

- A comparison between the overabundance obtained at the end of core He-burning in 25N and 25K shows that the reaction $^{12}\text{C}(\alpha, \gamma)^{16}\text{O}$ has only a small influence on the efficiency of the s-process during this phase. In contrast, the efficiency of the s-process during shell C-burning is very sensitive to the mass fraction of carbon left over at the end of core He-burning, which is determined by this reaction.
- The overabundances we have obtained in our case 25C at the end of core He-burning are similar to those calculated by Raiteri et al. (1991b). but our results of the shell C-burning are different from those by Raiteri et al. (1991b), since they have done essentially a one-zone calculation at fixed temperature and density.
- Table 4 indicates that the s-process during core He-burning leads to a monotonic increase of the overabundance as a function of stellar mass. However, this does not apply in the case of shell C-burning because branchings along the s-process path become effective as a result of the higher neutron density encountered during this phase (see Fig. 8). The behavior of the overabundance of $^{63,65}\text{Cu}$, ^{64}Zn , ^{80}Kr , $^{86,87}\text{Sr}$, and ^{152}Gd indicates this feature.

- In Table 6, we summarize the stellar yield compared to solar of the listed nuclei as obtained by integration above $1.5 M_{\odot}$ for each stellar mass. Their overproduction factor distribution as function of mass number A are plotted in Fig. 14. The dependence of this yield on the stellar mass reflects the behavior of the overabundance described above. Relatively high yield is obtained for the pure s-nuclei. We emphasize the remarkable difference by a factor 4.2 in the yield for ^{80}Kr resulting from the sequences 25N and 25K at the end of core oxygen burning. The reason is the destruction of ^{80}Kr by shell C-burning in the sequence 25N and its production in 25K. This is seen in Fig. 10, where the normalized mass fractions are displayed as a function of the interior mass in the sequences 25N and 25K at the end of core oxygen burning. Note also the difference in the mass fraction of ^{70}Zn between the two sequences, which we have attributed to the different neutron densities encountered during shell C-burning as discussed above in §4.
- It is quite remarkable that ^{152}Gd , produced abundantly (overabundance >18) during core helium burning in massive stars, is brought back to its solar value at the end of shell carbon burning due to the larger $^{152}\text{Eu}(n,\gamma)$ rate during shell carbon burning, which causes the s-process flow to bypass ^{152}Gd . This result is reasonable since s-processing in thermally-pulsed AGB stars produces enough ^{152}Gd to account for its solar abundance (Raiteri et al. 1993). A similar case also occurs for ^{158}Dy , which has an overabundance value of larger than 10 in all models studied at the end of core helium burning (Rayet & Hashimoto 2000) but decreases to an overabundance of less than solar after shell carbon burning. Production of ^{158}Dy occurs in the s-process because ^{157}Gd , which is stable in the lab, can β^- decay in stars. The rate for this decay is temperature and density dependent (Takahashi & Yokoi 1987). Interestingly, this rate is lower in the conditions of shell carbon burning than is core helium burning. Moreover, the neutron-capture rate for ^{157}Gd increases with the higher temperature and density of the carbon shell. These effects cause the s-process flow to bypass ^{158}Gd during carbon burning.
- The opposite case of ^{152}Gd is for isotope ^{116}Cd , which is destroyed almost completely during core helium burning to an overabundance of less than 0.002, but then reproduced to a value close to solar after shell carbon burning due to a higher neutron-capture rate of ^{115}Cd during shell carbon burning. A case similar to but less dramatic than ^{116}Cd is ^{96}Zr , which is destroyed during core helium burning to an overabundance ≤ 0.4 then recovers to an overabundance ≥ 1 at the end of shell carbon burning.
- An interesting feature of the s-process in shell carbon burning is the strong enhancement of ^{80}Se , ^{86}Kr , and ^{87}Rb to an overabundance larger than 10 from a value of ~ 1

at the end of core helium burning (see also Raiteri et al. 1993).

- Another significant feature of shell carbon burning is the overabundances of ^{23}Na and ^{27}Al . The overabundance of ^{23}Na is less than 10 at the end of core helium burning. It is enhanced significantly to a value larger than 230 in all models studied here. A similar result is also obtained for ^{27}Al overabundance which rises from 1.5 to 75.

8. Conclusions

Our detailed study of the s-process nucleosynthesis resulting from core He-burning and shell C-burning in massive stars on the basis of the updated nuclear data of some relevant reactions reveal many interesting points which we summarize in the following.

- The efficiency of s-process nucleosynthesis during core He-burning does not depend on the rate of $^{12}\text{C}(\alpha, \gamma)^{16}\text{O}$ but it is sensitive to the rates of $^{22}\text{Ne}(\alpha, n)^{25}\text{Mg}$ and $^{16}\text{O}(n, \gamma)^{17}\text{O}$. When we use the updated rates of these two reactions, as described in §2, we find a significantly reduced efficiency of the s-process during core He-burning (see Table 2).
- The s-process in shell C-burning is more complicated and depends on the evolution of the massive star beyond core He-burning. This complexity can be seen from the locations, the number of carbon convective shells, and the thickness of carbon convective shells in our models. These in turn are sensitive to the central carbon mass fraction X_{12} achieved at the end of core He-burning as a result of the reaction $^{12}\text{C}(\alpha, \gamma)^{16}\text{O}$, whose rate is not yet adequately determined. If this rate leads to a relatively lower X_{12} , then the s-process occurs later in time, possibly even after central neon burning. Consequently, the neutrons density achieved is high enough (see Fig. 8) to drive the nuclear reaction flow to the Zirconium region. This does not happen when X_{12} is higher, as in our case 25K, since the s-process occurs here earlier in time (before central neon ignition) and at lower temperatures and densities, which result in a smaller neutron density. This explains why the nuclear reaction flow stops essentially in the Strontium region.
- Our calculations show that the overabundance of ^{70}Zn can be used as indicator of the strength of the nuclear reaction flow through the branchings along the s-process path, especially at ^{69}Zn . We have also found that ^{87}Rb is strongly produced during shell carbon burning due to the higher rate of neutron-capture of ^{86}Rb relative to its rate during core helium burning (Raiteri et al. 1993).

- We measure the s-processing in the core helium, shell helium, and shell carbon burning in massive stars with $N_c = \int n_c(M_r) dM_r$ and show their relative strengths or importance. We show the s-process contribution from shell carbon burning decreases with increasing mass of the star.
- In comparing the yields of s-only nuclei of our stellar models with the solar distribution, we find that it is necessary to include the results of s-processing from shell carbon burning and to mix the yields of all mass range of massive stars to give a reasonable fit to the solar distribution. For s-only nuclei with mass number $A \leq 87$, massive stars contribute at least 40% to the solar s-only nuclei. For s-only nuclei with mass number $A > 90$, massive stars contribute on average $\sim 7\%$, except for ^{152}Gd , ^{187}Os , and ^{198}Hg which can be 14%, 13%, and 11%, respectively.

The authors are grateful to J. S. Brown for providing the equation of state tables. M.F. EL Eid thanks the American University of Beirut (AUB) for a URB grant to visit Clemson University during summer 2005. L.-S. The thanks the Aspen Institute of Physics for hospitality, support, and for organizing the 2005 workshop on the physics of s-process. L.-S. The also acknowledges valuable discussions with A. Burrows, D. Clayton, I. Dominguez, R. Gallino, A. Heger, F. Herwig, F. Kappeler, U. Ott, R. Reifarth, O. Straniero, and F.X.Timmes. This work has been supported by NSF grant AST-9819877 and by grants from NASA's Cosmochemistry Program and from the DOE's Scientific Discovery through Advanced Computing Program (grant DE-FC02-01ER41189).

REFERENCES

- Anders, E. & Grevesse, N. 1989, *Geochim. Cosmochim. Acta*, 53, 197
- Angulo, C., Arnould, M., Rayet, M., Descouvemont, P., Baye, D., Leclercq-Willain, C., Coc, A., Barhoumi, S., Aguer, P., Rolfs, C., Kunz, R., Hammer, J. W., Mayer, A., Paradellis, T., Kossionides, S., Chronidou, C., Spyrou, K., degl'Innocenti, S., Fiorentini, G., Ricci, B., Zavatarelli, S., Providencia, C., Wolters, H., Soares, J., Grama, C., Rahighi, J., Shotton, A., & Laméhi Rachti, M. 1999, *Nuclear Physics A*, 656, 3
- Arlandini, C., Käppeler, F., Wisshak, K., Gallino, R., Lugaro, M., Busso, M., & Straniero, O. 1999, *ApJ*, 525, 886

- Arnett, D. 1996, *Supernovae and nucleosynthesis. an investigation of the history of matter, from the Big Bang to the present* (Princeton series in astrophysics, Princeton, NJ: Princeton University Press, —c1996)
- Arnould, M. & Goriely, S. 2003, *Phys. Rep.*, 384, 1
- Audi, G. & Wapstra, A. H. 1995, *Nuclear Physics A*, 595, 409
- Baraffe, I., El Eid, M. F., & Prantzos, N. 1992, *A&A*, 258, 357
- Beer, H. 1986, in *Advances in Nuclear Astrophysics*, ed. E. Vangioni-Flam, J. Audouze, M. Casse, J.-P. Chieze, & J. Tran Thanh van, 375–383
- Beer, H. & Macklin, R. L. 1989, *ApJ*, 339, 962
- Beer, H., Voss, F., & Winters, R. R. 1992, *ApJS*, 80, 403
- Buchmann, L. 1996, *ApJ*, 468, L127
- Burbidge, E. M., Burbidge, G. R., Fowler, W. A., & Hoyle, F. 1957, *Rev. Mod. Phys.*, 29, 547
- Busso, M., Gallino, R., & Wasserburg, G. J. 1999, *ARA&A*, 37, 239
- Cameron, A. G. W. 1957, *PASP*, 69, 201
- Caughlan, G. R. & Fowler, W. A. 1988, *Atomic Data and Nuclear Data Tables*, 40, 283
- Chieffi, A., Limongi, M., & Straniero, O. 1998, *ApJ*, 502, 737
- Clayton, D. D. 1983, *Principles of stellar evolution and nucleosynthesis* (Chicago: University of Chicago Press, 1983)
- Clayton, D. D., Fowler, W. A., Hull, T. E., & Zimmerman, B. A. 1961, *Ann.Phys.*, 12, 331
- Clayton, D. D. & Rassbach, M. E. 1967, *ApJ*, 148, 69
- Cowley, C. R. 1995, *An introduction to cosmochemistry* (Cambridge; New York: Cambridge University Press, —c1995)
- de Jager, C., Nieuwenhuijzen, H., & van der Hucht, K. A. 1988, *A&AS*, 72, 259
- Drotleff, H. W., Denker, A., Knee, H., Soine, M., Wolf, G., Hammer, J. W., Greife, U., Rolfs, C., & Trautvetter, H. P. 1993, *ApJ*, 414, 735

- El Eid, M. F., Meyer, B. S., & The, L.-S. 2004, *ApJ*, 611, 396
- Federman, S. R., Knauth, D. C., & Lambert, D. L. 2004, *ApJ*, 603, L105
- Hartmann, D., Woosley, S. E., & El Eid, M. F. 1985, *ApJ*, 297, 837
- Howard, W. M., Arnett, W. D., Clayton, D. D., & Woosley, S. E. 1972, *ApJ*, 175, 201
- Igashira, M., Nagai, Y., Masuda, K., Ohsaki, T., & Kitazawa, H. 1995, *ApJ*, 441, L89
- Imbriani, G., Limongi, M., Gialanella, L., Terrasi, F., Straniero, O., & Chieffi, A. 2001, *ApJ*, 558, 903
- Jaeger, M., Kunz, R., Mayer, A., Hammer, J. W., Staudt, G., Kratz, K. L., & Pfeiffer, B. 2001, *Phys. Rev. Lett.*, 87, 202501
- Jordan, G. C., Meyer, B. S., & D’Azevedo, E. 2005, in *Open Issues in Supernovae*, ed. A. Mezzacappa & G. M. Fuller (World Scientific)
- Kappeler, F., Beer, H., & Wisshak, K. 1989, *Reports of Progress in Physics*, 52, 945
- Klay, N. & Käppeler, F. 1988, *Phys. Rev. C*, 38, 295
- Kunz, R., Fey, M., Jaeger, M., Mayer, A., Hammer, J. W., Staudt, G., Harissopulos, S., & Paradellis, T. 2002, *ApJ*, 567, 643
- Langer, N., Arcoragi, J.-P., & Arnould, M. 1989, *A&A*, 210, 187
- Limongi, M., Straniero, O., & Chieffi, A. 2000, *ApJS*, 129, 625
- Loss, R. D. & Lugmair, G. W. 1990, *ApJ*, 360, L59
- Meyer, B. S., Krishnan, T. D., & Clayton, D. D. 1996, *ApJ*, 462, 825
- Misawa, K., Shih, C.-Y., Reese, Y., Bogard, D. D., & Nyquist, L. E. 2006, *Earth and Planetary Science Letters*, 246, 90
- Nomoto, K. & Hashimoto, M. 1988, *Phys. Rep.*, 163, 11
- Prantzos, N., Arnould, M., & Arcoragi, J.-P. 1987, *ApJ*, 315, 209
- Prantzos, N., Hashimoto, M., & Nomoto, K. 1990, *A&A*, 234, 211
- Raiteri, C. M., Busso, M., Picchio, G., & Gallino, R. 1991a, *ApJ*, 371, 665
- Raiteri, C. M., Busso, M., Picchio, G., Gallino, R., & Pulone, L. 1991b, *ApJ*, 367, 228

- Raiteri, C. M., Gallino, R., Busso, M., Neuberger, D., & Kaeppler, F. 1993, *ApJ*, 419, 207
- Rauscher, T. & Thielemann, F. 2000, *Atomic Data and Nuclear Data Tables*, 75, 1
- Rayet, M. & Hashimoto, M. 2000, *A&A*, 354, 740
- Seeger, P. A., Fowler, W. A., & Clayton, D. D. 1965, *ApJS*, 11, 121
- Takahashi, K. & Yokoi, K. 1987, *Atomic Data and Nuclear Data Tables*, 36, 375
- The, L.-S., El Eid, M. F., & Meyer, B. S. 2000, *ApJ*, 533, 998
- Travaglio, C., Gallino, R., Arnone, E., Cowan, J., Jordan, F., & Sneden, C. 2004, *ApJ*, 601, 864
- Tuli, J. 1995, *Nuclear Wallet Cards* (Brookhaven: Brookhaven Natl. Lab.)
- Ulrich, R. K. 1973, in *Explosive Nucleosynthesis*, 139–167
- Volkening, J. & Papanastassiou, D. A. 1990, *ApJ*, 358, L29
- Woosley, S. E. 1997, *ApJ*, 476, 801
- Woosley, S. E., Heger, A., & Weaver, T. A. 2002, *Rev. Mod. Phys.*, 74, 1015

Table 1. Rates Used for Important Reactions in the Calculations

Model	$^{12}\text{C}(\alpha, \gamma)^{16}\text{O}$	$^{16}\text{O}(\text{n}, \gamma)^{17}\text{O}$	$^{22}\text{Ne}(\alpha, \text{n})^{25}\text{Mg}$
15N	NACRE	Igashira et al. (1995)	NACRE
20N	NACRE	Igashira et al. (1995)	NACRE
25C	CF88	Beer et al. (1992)	CF88
25K	Kunz et al. (2002)	Igashira et al. (1995)	NACRE
25N	NACRE	Igashira et al. (1995)	NACRE
30N	NACRE	Igashira et al. (1995)	NACRE
TEM00	CF88	BVW	CF88

Table 2. Comparison of s-Processing in Massive Stars during Core Helium Burning among different authors

Author	τ_c	n_c^a	$\langle \tau \rangle$ (mb^{-1}) ^b	n_n^{max} ($\times 10^5 \text{ cm}^{-3}$) ^c	X_{22} ($\times 10^{-2}$) ^d	$X_{80}/X_{80\odot}^e$
<u>15 M_\odot</u>						
K94	–	1.80	0.09	2.05	1.65	21
TEM00,A	4.00	3.38	0.10	2.27	1.33	117
Present Work, (15N)	1.79	1.19	0.06	0.89	1.50	15
<u>20 M_\odot</u>						
K94	–	3.66	0.15	5.06	1.32	116
TEM00,A	5.93	5.48	0.16	3.50	1.04	598
Present Work, (20N)	3.38	2.34	0.10	1.63	1.12	56
<u>25 M_\odot</u>						
K94	–	5.41	0.20	6.62	1.00	475
TEM00,A	7.15	6.70	0.22	4.24	0.76	1100
Present Work, (25C)	5.43	5.14	0.30	1.95	0.98	618
Present Work, (25N)	4.81	3.52	0.15	2.60	0.77	174
Present Work, (25K)	5.00	3.63	0.15	2.53	0.78	186
Present Work, (25NM)	5.19	4.03	0.17	2.50	0.58	264
<u>30 M_\odot</u>						
K94	–	6.55	0.23	6.74	0.79	933
TEM00,A	8.09	7.63	0.22	4.44	0.65	1368
Present Work, (30N)	5.94	4.24	0.14	1.84	0.54	352

^aNumber of neutrons captured per iron seed averaged over the maximum convective core mass.

^bMean neutron exposure at 30 keV averaged over the convective core mass.

^cMaximum of the mean neutron density.

^dFinal ^{22}Ne mass fraction.

^eFinal ^{80}Kr production factor averaged over the maximum convective core mass.

Table 3. Overabundance factors (X/X_{\odot}) resulting from the s-process calculation of the present work compared to Raiteri et al. (1991b,a), referred to as R(91b) and R(91a)

species	Z	End Core Helium				C-Shell			
		25N	25K	25C	R(91b)	25N	25K	25C	R(91a)
²³ Na	11	6.97	7.01	7.70	...	235	315	240	...
²⁷ Al	13	1.16	1.15	0.91	...	103	143	95.4	...
³⁷ Cl	17	72.1	72	72.5	65.8	61.1	61.8	62	...
⁴⁰ K	19	268	284	332	291.7	224	255	280	...
⁵⁰ Ti	22	158	158	19.7	15.9	16.9	16.4	21.4	...
⁵⁴ Cr	24	16.8	15.8	16.2	16.5	16.4	16.4	15.3	...
⁵⁸ Fe	26	105	104	90	84	92.8	93.1	76.1	56.7
⁵⁹ Co	27	36.4	36.5	34	35.9	39.2	45.5	33.3	...
⁶¹ Ni	28	53.8	55.2	61	84.6	60.4	67.9	68	...
⁶² Ni	28	31.6	32.7	40	49.9	34.4	36.6	40.2	...
⁶⁴ Ni	28	56.6	59.1	95.6	164.5	109	115	153	...
⁶³ Cu	29	58.3	60.8	78.2	91.8	11.5	64.6	42.9	...
⁶⁵ Cu	29	122	128	205	226.3	83.5	148	175	...
⁶⁴ Zn	30	29.4	30.7	43.6	41	8.6	23.2	22.5	...
⁶⁶ Zn	30	57	59.6	107	118.9	62.1	80.6	121	...
⁶⁷ Zn	30	79.4	82.9	153	171.7	137	160	256	...
⁶⁸ Zn	30	70	73.1	158	164.7	128	131	237	...
⁷⁰ Zn	30	0.38	0.38	0.56	–	39.9	4.7	31.7	...
⁷⁰ Ge	32	107	112	270	253.7	217	216	402	527.1
⁷² Ge	32	72.2	75.2	201	190.7	187	158	385	...
⁷³ Ge	32	45.1	46.9	128	128.8	180	147	357	...
⁷⁴ Ge	32	35.9	37.5	110	99.3	101	84.9	204	...
⁷⁵ As	33	26.3	27.4	81.9	59.6	99.1	75.4	189	...
⁷⁶ Se	34	74.7	78.2	241	212	189	164	357	763.1
⁸⁰ Se	34	1.21	1.29	3.95	...	54.7	56.3	...	763.1
⁸⁰ Kr	36	174	183	618	480.7	45.2	354	367	675.6
⁸² Kr	36	73.4	77.9	277	210.3	124	181	485	495.9
⁸⁶ Kr	36	2.57	2.63	5.72	...	50.9	10.4	44.3	224.3
⁸⁷ Rb	37	1.26	1.27	3.03	...	55.4	43.3	233	292.3
⁸⁶ Sr	38	57.1	60.7	232	147	20.7	138	316	147.4
⁸⁷ Sr	38	47.3	50.4	190	129	28.3	108	378	57.3
⁸⁸ Sr	38	14.1	14.9	45.3	...	20.1	27.7	99.6	...
⁹⁶ Zr	40	0.19	0.19	0.12	...	11.3	1.18	3.87	...
¹¹⁶ Cd	48	0.001	0.001	0.001	...	2.67	0.34	4.44	...
¹⁵² Gd	64	22.8	22.9	31.8	38.6	0.09	8.24	1.19	29.2
¹⁵⁸ Dy	66	14.9	11.5	21.4	...	0.04	0.38	0.87	...

Table 3—Continued

species	Z	End Core Helium				C-Shell			
		25N	25K	25C	R(91b)	25N	25K	25C	R(91a)

Table 4. Overabundance of some relevant isotopes in He-Core and C-shell of our stellar models.

Isotope	Z	Core Helium Burning				Carbon Shell Burning			
		15N	20N	25N	30N	15N	20N	25N	30N
²³ Na	11	6.14	6.77	6.97	6.98	311.92	342.2	235.02	240.13
²⁷ Al	13	0.89	0.99	1.16	1.31	83.61	110.03	103.11	126.31
³⁷ Cl	17	58.78	69.29	72.12	72.69	57.65	62.22	61.14	58.47
⁴⁰ K	19	154.13	216.89	267.58	299.45	146.56	190.70	224.21	277.73
⁵⁰ Ti	22	9.78	13.63	15.84	17.42	11.55	14.81	16.89	18.16
⁵⁴ Cr	24	13.03	16.15	16.84	16.76	15.09	16.74	16.45	16.15
⁵⁸ Fe	26	82.03	106.33	104.89	98.54	98.23	102.28	92.78	88.76
⁵⁹ Co	27	19.68	32.95	36.43	36.18	39.66	46.76	39.25	40.23
⁶¹ Ni	28	19.96	39.98	53.82	59.59	39.54	61.78	60.39	68.44
⁶² Ni	28	9.53	21.10	31.55	37.34	17.74	30.25	34.42	38.32
⁶⁴ Ni	28	11.10	31.27	56.63	76.70	48.56	95.50	109.32	116.65
⁶³ Cu	29	16.16	37.42	58.32	70.70	33.12	48.55	11.48	45.89
⁶⁵ Cu	29	23.37	67.45	122.41	165.68	42.18	95.37	83.51	158.52
⁶⁴ Zn	30	6.79	17.44	29.40	37.72	5.47	14.51	8.61	21.91
⁶⁶ Zn	30	8.45	28.59	56.97	81.94	21.17	49.73	62.10	96.00
⁶⁷ Zn	30	10.85	38.69	79.37	116.15	40.82	96.97	136.82	197.35
⁶⁸ Zn	30	7.42	30.19	70.13	111.04	29.29	76.69	128.42	161.20
⁷⁰ Zn	30	0.51	0.38	0.38	0.41	2.65	3.87	39.94	6.16
⁷⁰ Ge	32	9.83	42.61	107.36	178.42	44.89	124.58	217.37	270.10
⁷² Ge	32	5.96	25.98	72.22	128.22	32.49	89.61	186.75	207.79
⁷³ Ge	32	3.59	15.86	45.12	81.42	29.93	82.63	179.56	196.67
⁷⁴ Ge	32	2.88	12.09	35.86	67.27	16.50	46.90	100.75	109.58
⁷⁵ As	33	2.09	8.77	26.29	49.76	14.58	40.43	99.09	96.53
⁷⁶ Se	34	6.01	24.58	74.75	143.74	31.08	89.80	188.51	209.01
⁸⁰ Se	34	0.15	0.39	1.21	2.51	4.75	8.09	54.71	27.70
⁸⁰ Kr	36	15.24	55.70	174.25	352.13	49.58	182.40	45.16	316.64
⁸² Kr	36	7.83	23.59	73.44	153.31	26.29	93.21	123.66	204.95
⁸⁶ Kr	36	0.94	1.34	2.57	4.92	3.71	5.88	50.92	16.33
⁸⁷ Rb	37	0.72	0.84	1.26	2.21	17.83	27.23	55.45	76.23
⁸⁶ Sr	38	11.99	22.61	57.07	121.10	24.79	61.24	20.71	152.34
⁸⁷ Sr	38	11.14	20.28	47.27	98.75	22.00	49.36	28.32	150.39
⁸⁸ Sr	38	3.70	7.53	14.11	25.13	7.89	14.45	20.07	40.14
⁹⁶ Zr	40	0.42	0.27	0.20	0.16	1.12	1.14	11.30	1.93
¹¹⁶ Cd	48	0.0002	0.001	0.001	0.002	0.55	0.30	2.67	0.47
¹⁵² Gd	64	17.65	18.81	22.76	27.04	2.38	3.74	0.09	0.91
¹⁵⁸ Dy	66	7.52	10.90	14.91	18.71	0.35	0.14	0.04	0.64

Table 5. Properties of s-processing during Shell Carbon Burning

Model	$\Delta M_{C\text{-Shell}}^a$ (M_\odot)	τ_{CB}^b (yrs)	T_9^c	ρ_5^d	$\Delta\tau_n^e$ (mb^{-1})	Δn_c^f	$\langle \Delta\tau \rangle^g$ (mb^{-1})	$n_{10}^{max\ h}$	X_{22}^i ($\times 10^{-3}$)	\mathcal{O}_{80}^j	$\mathcal{O}_{88}^{j,k}$
15N	1.38 - 1.98	1.07	1.07	1.81	0.20	1.04	0.038	3.9	3.10	28	7.59
20N	1.24 - 3.12	21.1	0.97	1.10	0.71	1.22	0.049	1.0	0.88	177	14.0
25C	1.23 - 4.00	12.0	1.01	0.98	0.80	1.32	0.042	1.3	1.06	911	97.4
25K	1.30 - 4.54	20.3	1.02	0.91	0.83	1.02	0.036	1.1	0.37	352	27.7
25N	2.26 - 4.94	0.46	1.15	1.14	1.10	0.47	0.038	70	0.67	45	20.1
25NM	1.21 - 3.50	4.12	1.08	1.30	0.40	1.14	0.079	1.8	0.81	108	44.7
30N	1.33 - 5.22	4.06	1.13	1.10	0.56	0.61	0.019	4.3	0.80	311	46.9

^aThe interior mass range of the last carbon shell.

^bThe duration of the shell carbon burning.

^cThe average temperature weighted by its neutron exposure at the bottom of the carbon shell in 10^9 K.

^dThe average density weighted by its neutron exposure at the bottom of the carbon shell in 10^5 gm cm^{-3} .

^eThe increase of the neutron exposure at the bottom of the carbon shell.

^fThe increase of the number of neutron captures per iron seed averaged over the convective shell.

^gThe increase of the neutron exposure averaged over the convective shell.

^hThe maximum neutron density at the bottom of the carbon shell in 10^{10} cm^{-3} .

ⁱThe mass fraction of ^{22}Ne at the end of the burning shell.

^jThe overabundance of ^{80}Kr and ^{88}Sr isotopes relative to their solar abundance.

^kFor comparison, the overabundances of ^{88}Sr at the end of core helium burning for model 15N, 20N, 25C, 25K, 25NM, and 30N are 3.46, 7.17, 43.0, 14.4, 13.4, 19.1, and 23.8 respectively.

Table 6. Stellar yield (X/X_{\odot} with mass cut at $M_r=1.5 M_{\odot}$) of some heavy isotopes at the end of core Oxygen burning

Isotope	Z	X/X_{\odot}				
		15N	20N	25N	25K	30N
¹¹ Na	11	14.60	32.61	36.20	37.61	25.01
¹³ Al	13	4.33	11.12	15.82	19.81	19.61
³⁷ Cl	17	5.44	9.65	11.52	11.67	13.81
⁴⁰ K	19	13.30	27.89	39.55	44.95	61.42
⁵⁰ Ti	22	1.68	2.66	3.45	3.42	4.51
⁵⁴ Cr	24	2.06	3.10	3.60	3.64	4.37
⁵⁸ Fe	26	7.04	13.78	16.19	16.39	21.15
⁵⁹ Co	27	3.04	6.09	7.39	7.44	7.79
⁶¹ Ni	28	3.44	7.75	10.33	11.27	13.90
⁶² Ni	28	2.05	4.17	7.52	7.32	9.65
⁶⁴ Ni	28	3.60	10.07	17.11	17.39	22.81
⁶³ Cu	29	2.62	6.32	3.42	9.43	9.61
⁶⁵ Cu	29	3.61	11.14	15.31	22.05	28.26
⁶⁴ Zn	30	1.38	2.61	2.52	4.31	5.29
⁶⁶ Zn	30	2.31	6.01	12.21	13.97	18.29
⁶⁷ Zn	30	3.32	10.40	20.88	23.59	31.57
⁶⁸ Zn	30	2.78	8.36	21.39	19.91	31.93
⁷⁰ Zn	30	1.05	1.22	5.74	2.00	4.92
⁷⁰ Ge	32	3.77	12.85	33.15	32.93	47.42
⁷² Ge	32	2.96	9.34	32.52	27.23	45.71
⁷³ Ge	32	2.55	8.43	25.08	21.78	31.35
⁷⁴ Ge	32	1.95	5.25	16.12	13.13	25.41
⁷⁵ As	33	1.76	4.64	16.23	11.54	13.94
⁷⁶ Se	34	3.04	9.40	29.33	29.18	34.34
⁸⁰ Se	34	1.20	1.61	7.92	3.21	8.46
⁸⁰ Kr	36	4.14	17.93	11.29	47.72	47.35
⁸² Kr	36	2.76	9.72	20.82	28.41	35.43
⁸⁶ Kr	36	1.24	1.45	8.10	2.72	8.21
⁸⁷ Rb	37	1.69	3.28	10.55	7.58	15.93
⁸⁶ Sr	38	2.47	7.26	6.33	19.91	23.10
⁸⁷ Sr	38	2.22	5.74	6.53	15.79	22.89
⁸⁸ Sr	38	1.40	2.36	4.40	5.18	8.33
⁹⁶ Zr	40	0.98	0.98	2.18	1.02	1.30
¹¹⁶ Cd	48	0.92	0.86	1.12	0.85	1.02
¹⁵² Gd	64	3.66	3.15	1.78	3.34	2.44
¹⁵⁸ Dy	66	1.06	1.02	0.99	0.99	2.07

Table 7. Measuring s-process Production of Core Helium, Shell Helium, and Shell Carbon Burning in Massive Stars

Model	$N_c^a(\text{He-core})$	$N_c(\text{He-shell})$	$N_c(\text{C-shell})$	$N_c(\text{Total})$
15N	0.75	0.24	0.90	1.90
20N	5.01	0.27	2.27	7.54
25C	19.3	0.54	4.96	24.8
25K	13.3	0.28	3.39	17.0
25N	12.9	0.32	2.48	15.7
25NM	14.5	0.36	2.28	17.1
30N	23.9	0.72	4.33	29.0

^a $N_c = \int n_c(M_r) dM_r$, where n_c is the number of neutron captures per iron seed nuclei, and integration is over the mass range (in unit of M_\odot) of the relevant convective burning regions and above the mass cut, $1.5 M_\odot$

Table 8. s-process Contribution to Solar Abundances

Isotope	Z	Overproduction factor X/X_{\odot}				
		Weak Comp. (25N)	Weak Comp. (25K)	Main Comp.	Total (25N) ^a	Total (25K) ^b
²³ Na	11	1.21	1.14
²⁷ Al	13	0.57	0.56
³⁷ Cl	17	0.46	0.43
⁴⁰ K	19	1.63	1.56
⁵⁰ Ti	22	0.14	0.13
⁵⁴ Cr	24	0.15	0.14
⁵⁸ Fe	26	0.67	0.62
⁵⁹ Co	27	0.28	0.26
⁶¹ Ni	28	0.40	0.38
⁶² Ni	28	0.26	0.24
⁶⁴ Ni	28	0.60	0.56
⁶³ Cu	29	0.26	0.29	0.00	0.27	0.30
⁶⁵ Cu	29	0.67	0.67	0.01	0.68	0.68
⁶⁴ Zn	30	0.14	0.14	0.00	0.14	0.14
⁶⁶ Zn	30	0.44	0.42	0.01	0.45	0.43
⁶⁷ Zn	30	0.74	0.71	0.02	0.76	0.73
⁶⁸ Zn	30	0.72	0.66	0.03	0.75	0.69
⁷⁰ Zn	30	0.14	0.10	0.00	0.14	0.10
⁶⁹ Ga	31	0.78	0.72	0.04	0.82	0.76
⁷¹ Ga	31	0.77	0.85	0.06	0.82	0.90
⁷⁰ Ge	32	1.08	1.00	0.07	1.14	1.07
⁷² Ge	32	1.00	0.89	0.08	1.07	0.96
⁷³ Ge	32	0.74	0.66	0.05	0.79	0.71
⁷⁴ Ge	32	0.55	0.48	0.06	0.60	0.54
⁷⁵ As	33	0.39	0.33	0.05	0.44	0.37
⁷⁶ Se	34	0.83	0.77	0.15	0.98	0.92
⁷⁸ Se	34	0.62	0.55	0.11	0.72	0.65
⁸⁰ Se	34	0.21	0.16	0.09	0.30	0.25
⁸⁰ Kr	36	0.96	1.17	0.12	1.07	1.29
⁸² Kr	36	0.77	0.78	0.37	1.13	1.14
⁸⁶ Kr	36	0.21	0.15	0.27	0.47	0.41
⁸⁷ Rb	37	0.35	0.31	0.35	0.70	0.65
⁸⁶ Sr	38	0.47	0.54	0.47	0.92	1.00
⁸⁷ Sr	38	0.44	0.48	0.50	0.93	0.98
⁸⁸ Sr	38	0.19	0.18	0.92	1.08	1.08
⁹⁶ Zr	40	0.06	0.05	0.55	0.60	0.58
⁹⁶ Mo	42	0.07	0.06	1.03	1.10	1.10
¹⁰⁰ Ru	44	0.06	0.06	0.95	0.99	0.99
¹⁰⁴ Pd	46	0.06	0.06	1.06	1.09	1.09
¹¹⁰ Cd	48	0.06	0.05	0.97	1.00	1.00
¹¹⁶ Cd	48	0.05	0.04	0.18	0.22	0.21
¹¹⁶ Sn	50	0.05	0.05	0.86	0.89	0.89
¹²² Te	52	0.05	0.05	0.88	0.91	0.91
¹²³ Te	52	0.05	0.05	0.89	0.93	0.92

Table 8—Continued

Isotope	Z	Overproduction factor X/X_{\odot}				
		Weak Comp. (25N)	Weak Comp. (25K)	Main Comp.	Total (25N) ^a	Total (25K) ^b
¹²⁴ Te	52	0.06	0.05	0.91	0.94	0.94
¹²⁸ Xe	54	0.06	0.06	0.82	0.86	0.86
¹³⁰ Xe	54	0.07	0.07	0.83	0.88	0.88
¹³⁴ Ba	56	0.07	0.07	0.98	1.03	1.03
¹³⁶ Ba	56	0.07	0.07	1.00	1.05	1.05
¹⁴² Nd	60	0.06	0.06	0.92	0.96	0.96
¹⁴⁸ Sm	62	0.05	0.05	0.97	0.99	0.99
¹⁵⁰ Sm	62	0.06	0.06	1.00	1.03	1.03
¹⁵² Gd	64	0.14	0.14	0.88	1.00	1.00
¹⁵⁴ Gd	64	0.06	0.06	0.95	0.99	0.99
¹⁵⁸ Dy	66	0.06	0.06
¹⁶⁰ Dy	66	0.07	0.06	0.87	0.92	0.92
¹⁶⁴ Er	68	0.08	0.08	0.83	0.88	0.88
¹⁷⁰ Yb	70	0.08	0.08	1.01	1.07	1.07
¹⁷⁶ Lu	71	0.08	0.07	1.25	1.30	1.30
¹⁷⁶ Hf	72	0.07	0.07	0.96	1.01	1.01
¹⁸⁶ Os	76	0.06	0.05	0.97	1.00	1.00
¹⁸⁷ Os	76	0.13	0.12	0.82	0.92	0.92
¹⁹² Pt	78	0.08	0.08	0.98	1.04	1.04
¹⁹⁸ Hg	80	0.11	0.10	1.02	1.10	1.10
²⁰⁴ Pb	82	0.08	0.07	0.94	1.00	0.99
²⁰⁸ Pb	82	0.05	0.05	0.34	0.39	0.39

^aThe values of main component is scaled by a factor of 0.974 in order to produce the best fit to the s-only solar abundance

^bThe values of main component is scaled by a factor of 0.976 in order to produce the best fit to the s-only solar abundance

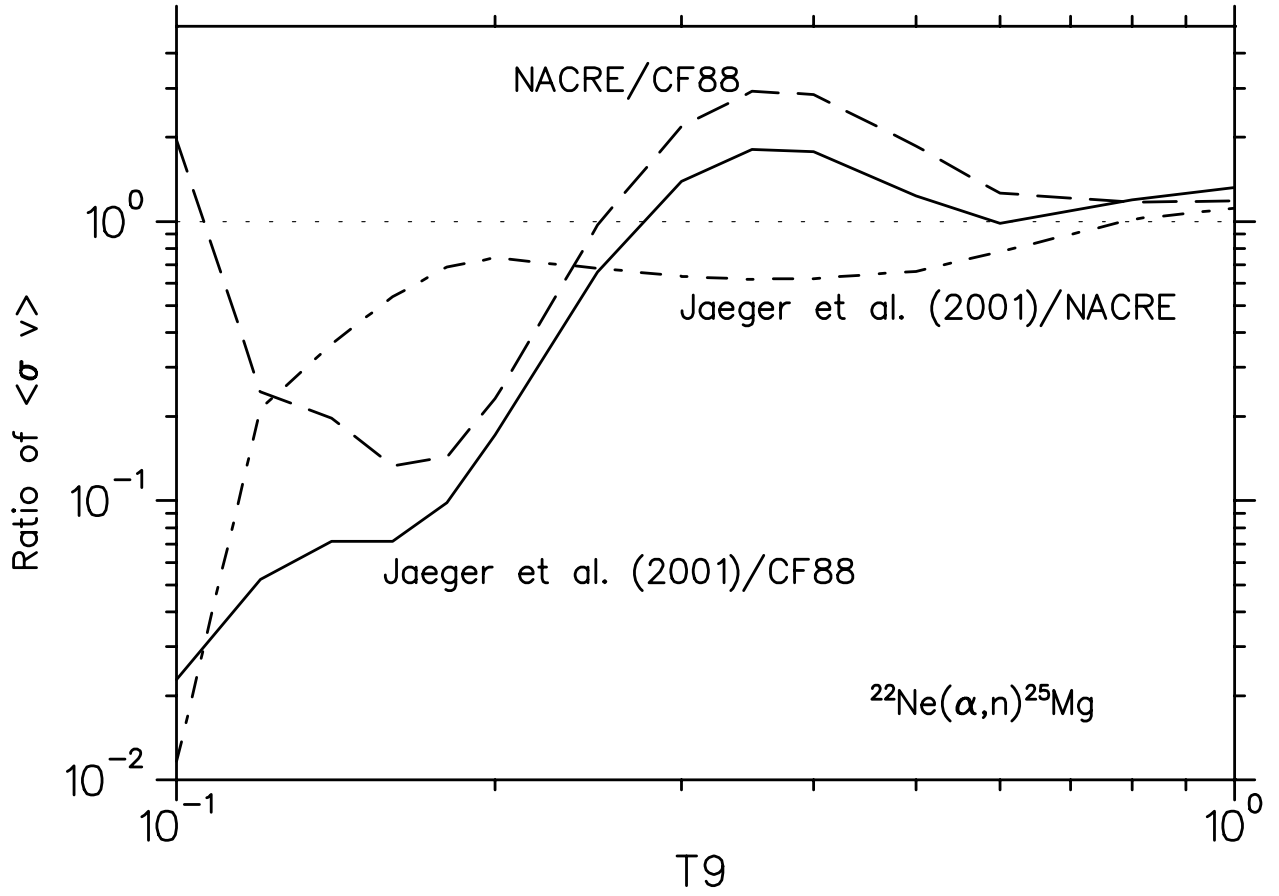


Fig. 1.— The $^{22}\text{Ne}(\alpha, n)^{25}\text{Mg}$ rate among different evaluations relative to CF88 or NACRE. See text for references.

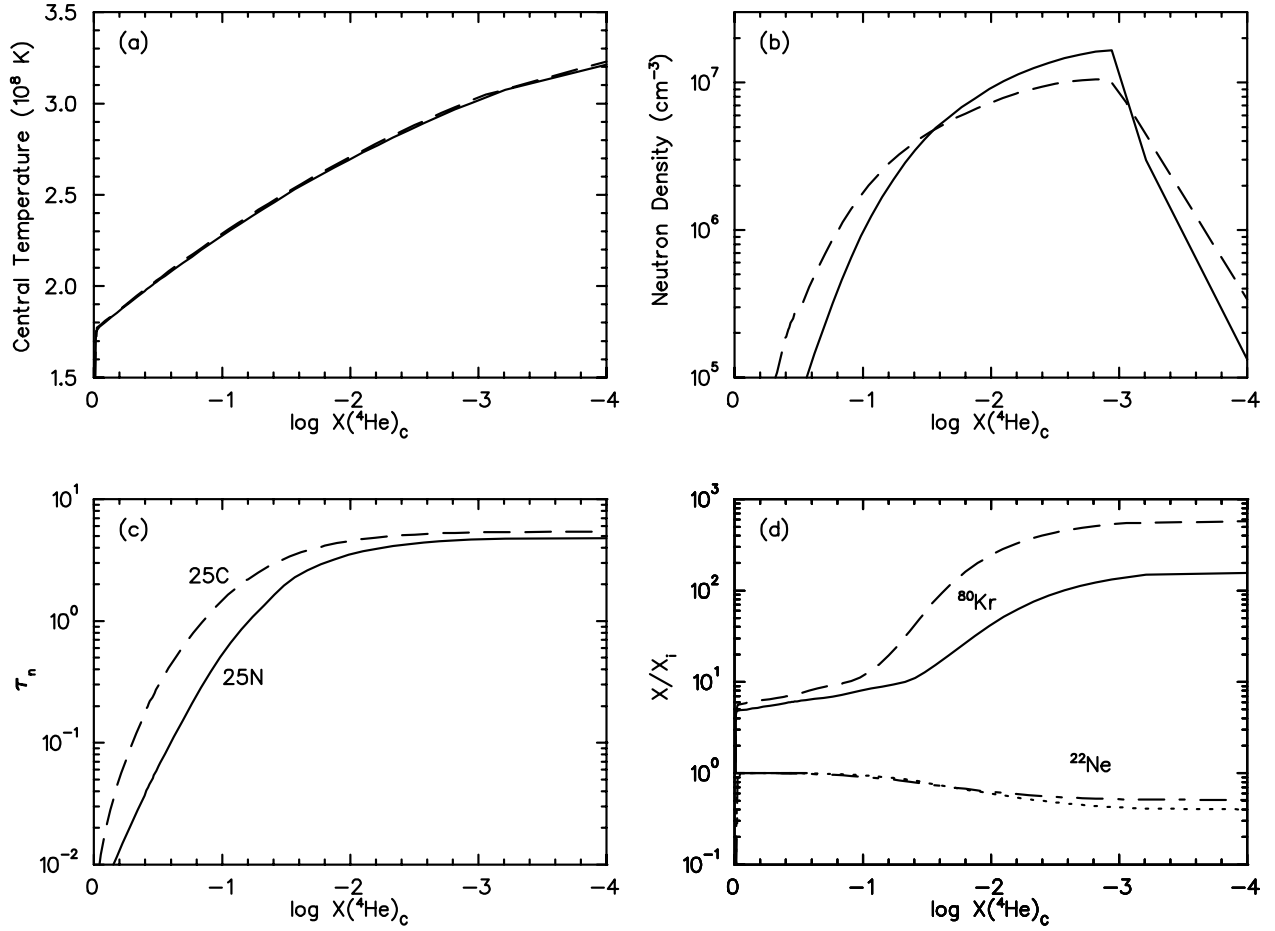


Fig. 2.— Some characteristics of the s-process during core He-burning according to the present work for a $25 M_{\odot}$ star in the cases 25N and 25C. τ_n is the neutron exposure experienced by a nucleus that remained at the center of the star at all times: $\tau_n = \int n_n v_{th} dt$, where n_n and v_{th} are the neutron density and thermal velocity of the neutrons at the center of the star. X/X_i is the ratio of the mass fraction to the mass fraction at the beginning of core helium burning.

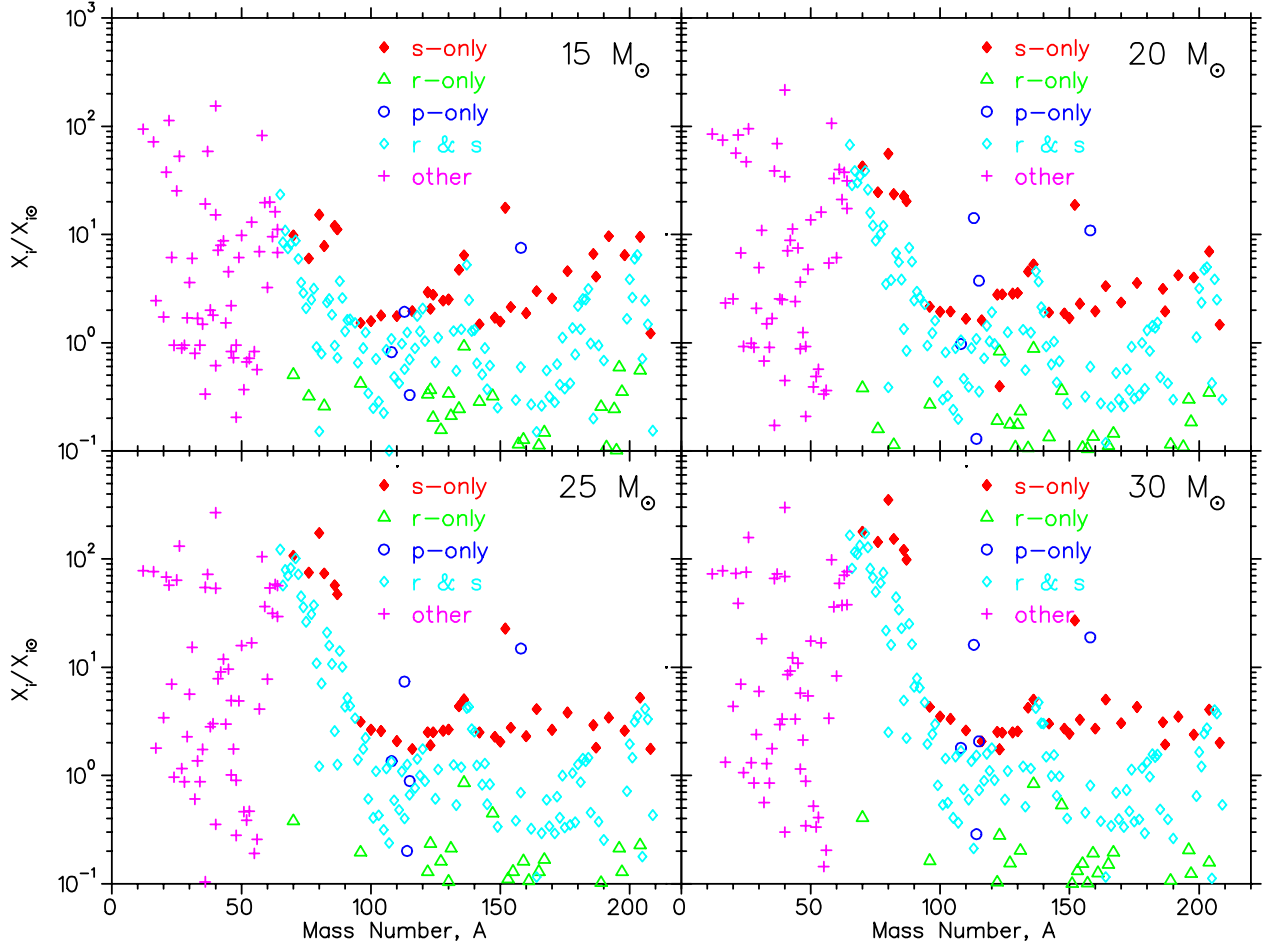


Fig. 3.— Overabundance factors of heavy nuclei averaged over the convective helium burning core for model 15N, 20N, 25N, and 30N. The primary nucleosynthesis production process for each nuclei is indicated by the symbol type.

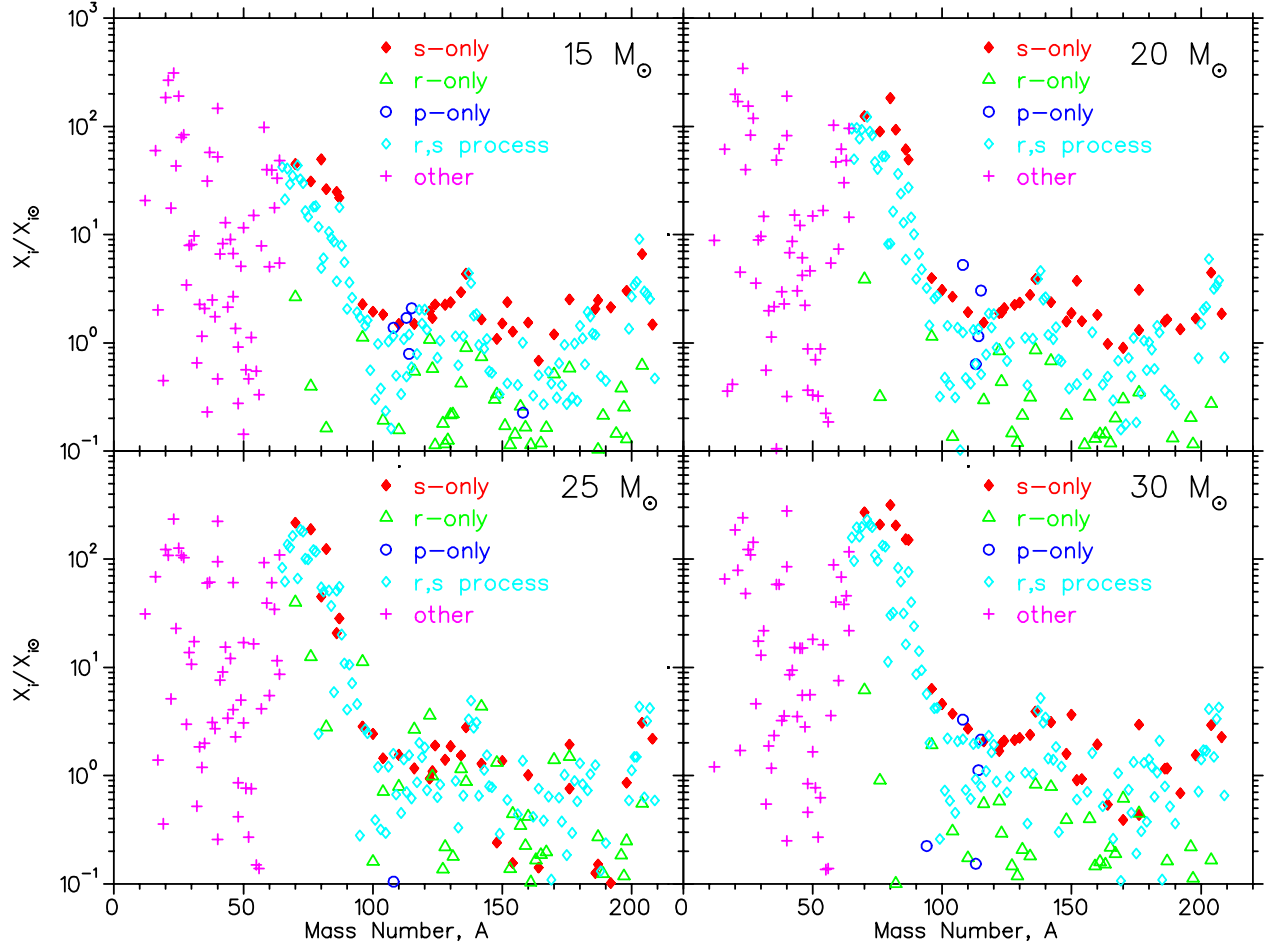


Fig. 4.— Similar to Fig. 3 but for the convective carbon burning shell model 15N, 20N, 25N, and 30N.

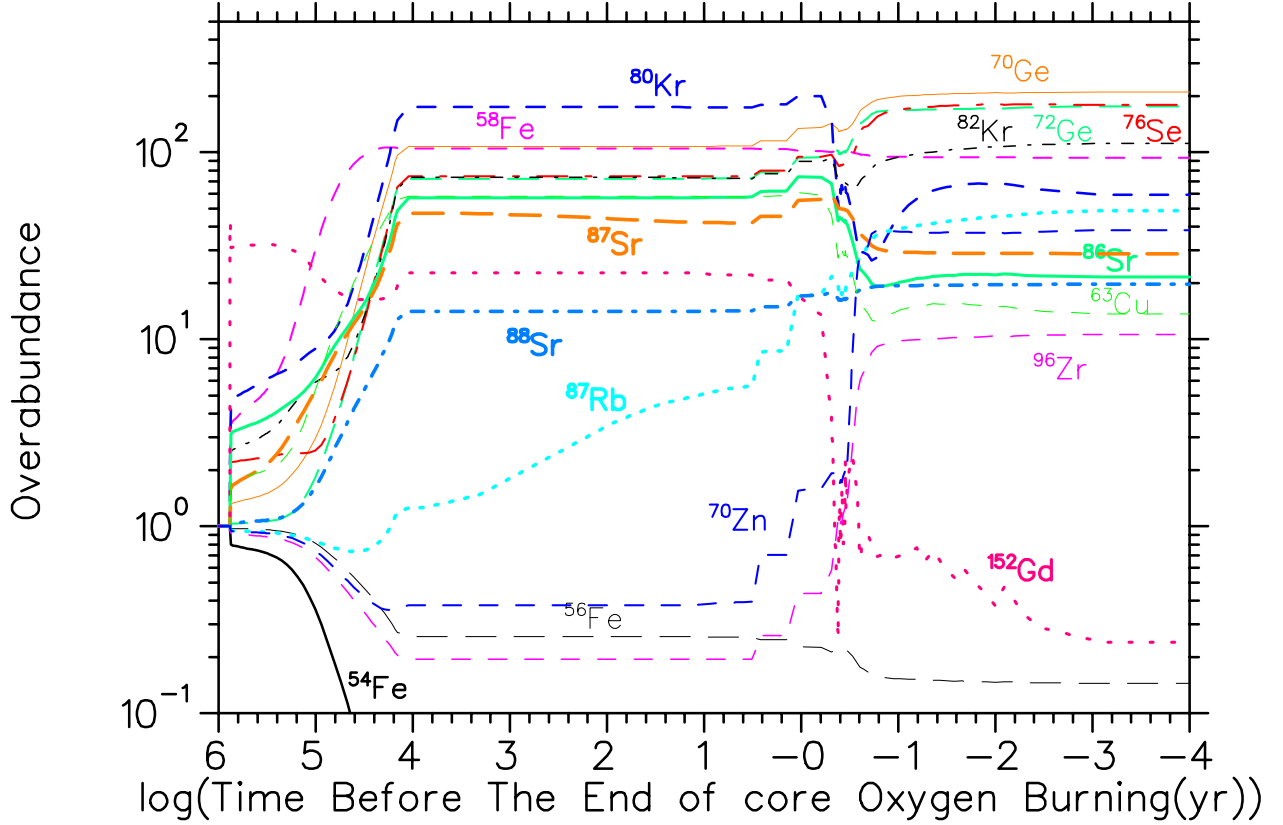


Fig. 5.— Overabundance factors of several nuclei produced as a function of time by the s-process during core helium burning and shell carbon-burning in a $25 M_{\odot}$ star, model 25N. These factors are taken at mass coordinate of $2.26 M_{\odot}$ specifying the bottom of the convective carbon-burning shell in this case. Core helium burning commences at abscissa value +6.0 and ends at +4.0. The first noticeable change occurs near the end of core helium burning, while the second change (abscissa value between 0.0 and -1.0) is the result of shell carbon-burning. An exception is ^{87}Rb which increases steadily between the two burning phases due to decay of ^{87}Sr (see text for explanation).

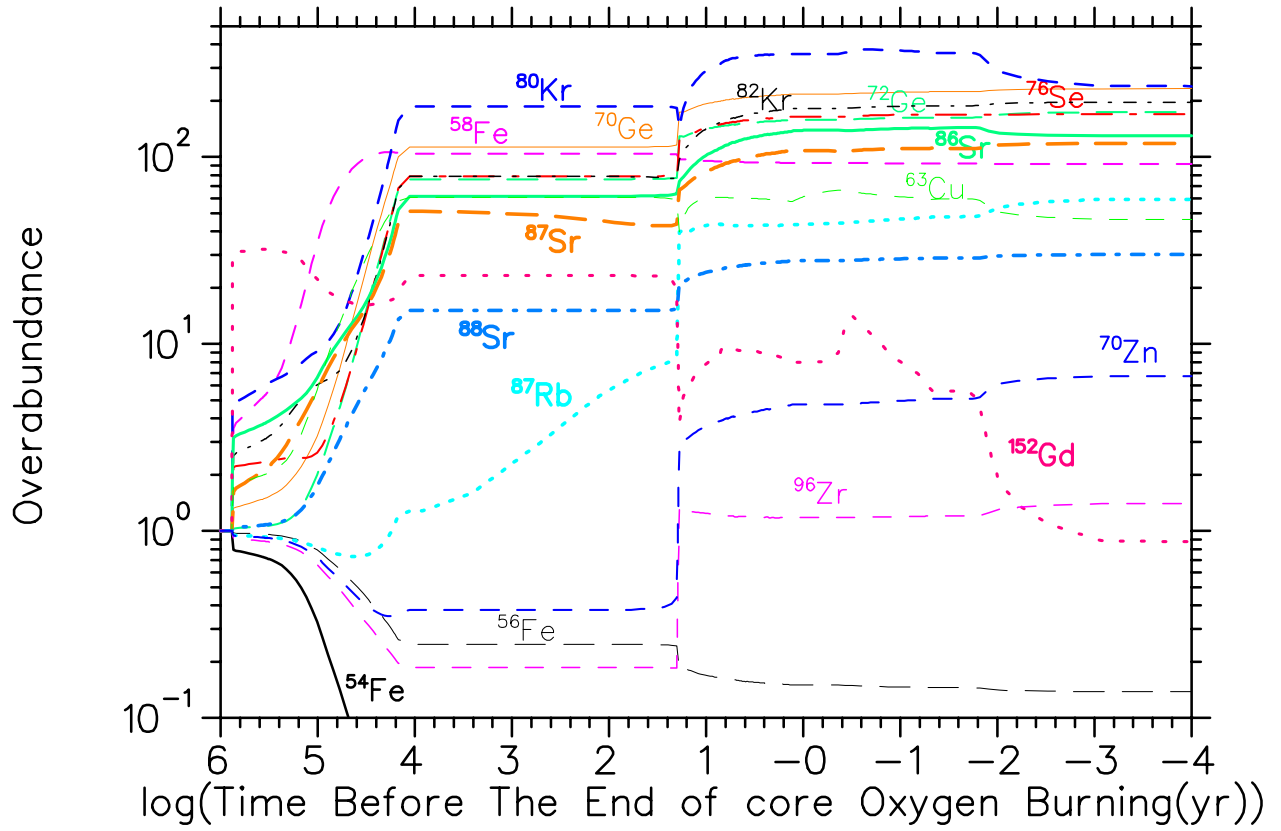


Fig. 6.— The same as Fig.4 but for the case 25K in our calculations. The overabundance values are determined at mass coordinate $2.0 M_{\odot}$ in this case.

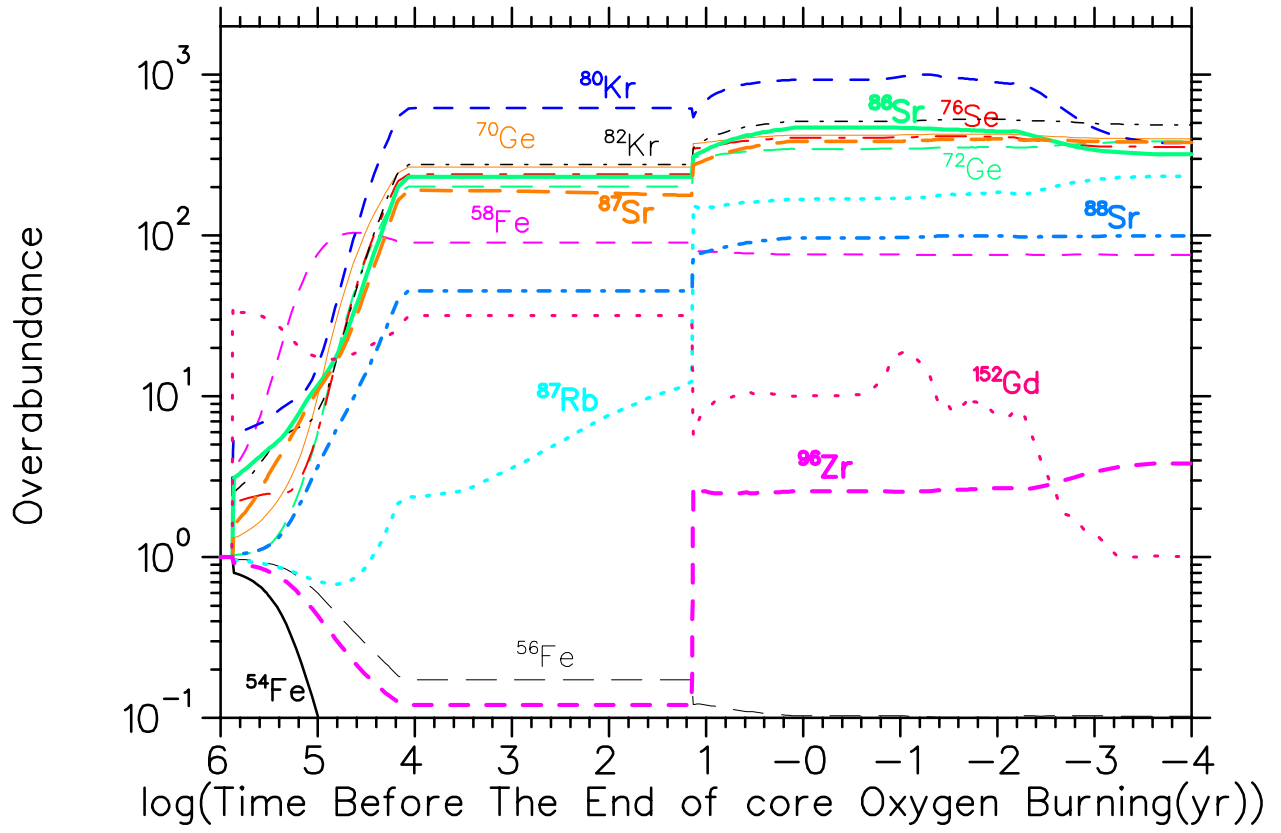


Fig. 7.— The same as Fig.4 but for the case 25C in our calculations. The overabundance values are taken at mass coordinate $2.547 M_{\odot}$.

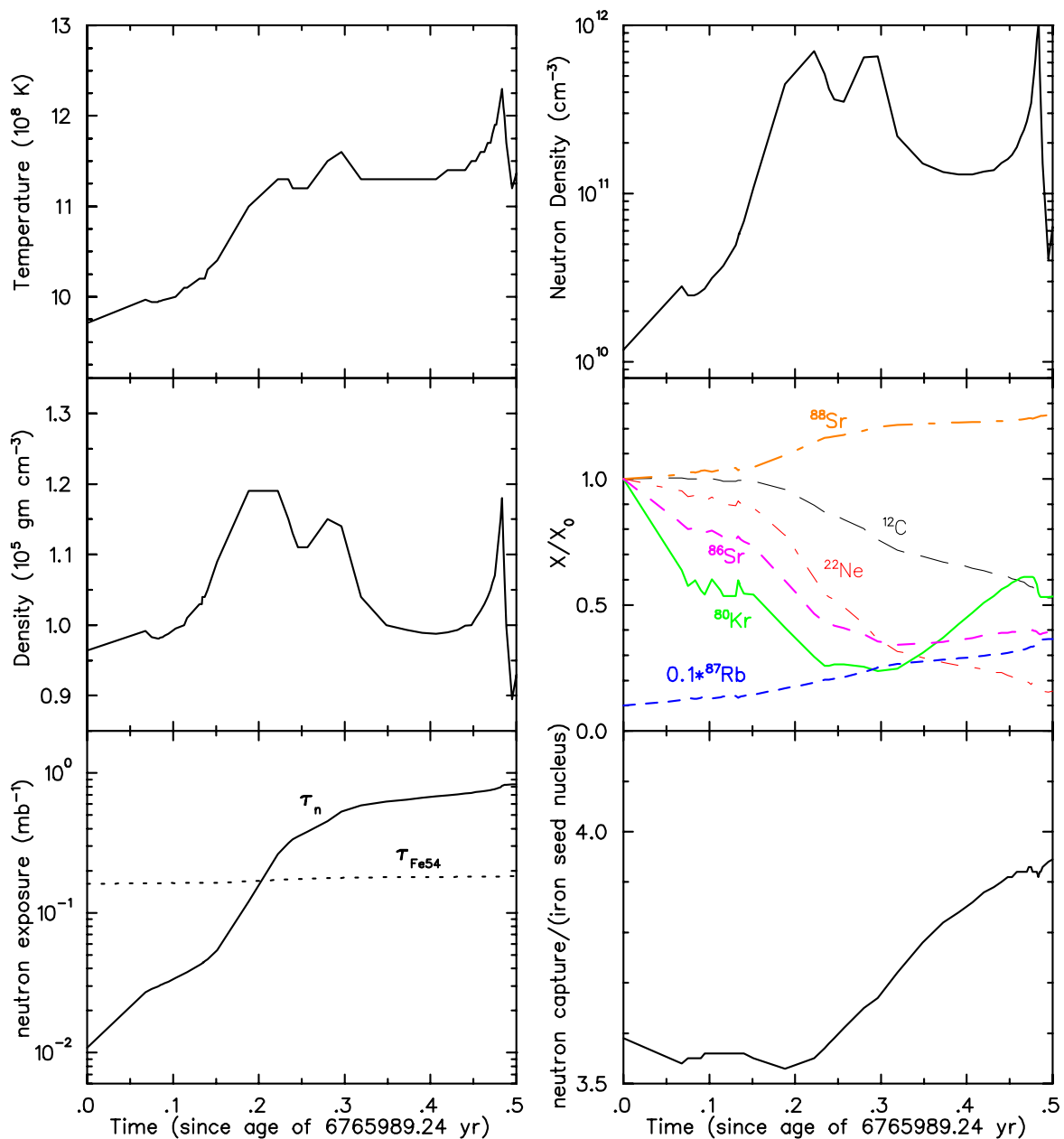


Fig. 8.— Several physical variables characterizing the carbon-burning shell in the sequence 25N. The panels display snapshots taken at mass coordinate $M_r=2.26 M_\odot$, which locates the bottom of the carbon-burning shell in this sequence of models. Note the gradual increase of the neutron density following the gradual change of temperature and density. X_0 is the mass fraction at the beginning of the shell C-burning. τ_n is the neutron exposure of the shell coordinate seen by a nucleus if it stays at this position at all times. τ_{Fe54} is the neutron exposure implied by the mass fraction of ^{54}Fe : $\tau_{\text{Fe54}} = -\ln(X_{54}/X_{54}^0)/\sigma_T$ where σ_T is the neutron-capture cross section at $T=30$ keV and X_{54} , X_{54}^0 are the final and initial mass fraction of ^{54}Fe , respectively. τ_{Fe54} is useful as a measure of the neutron exposure averaged over the convective zones.

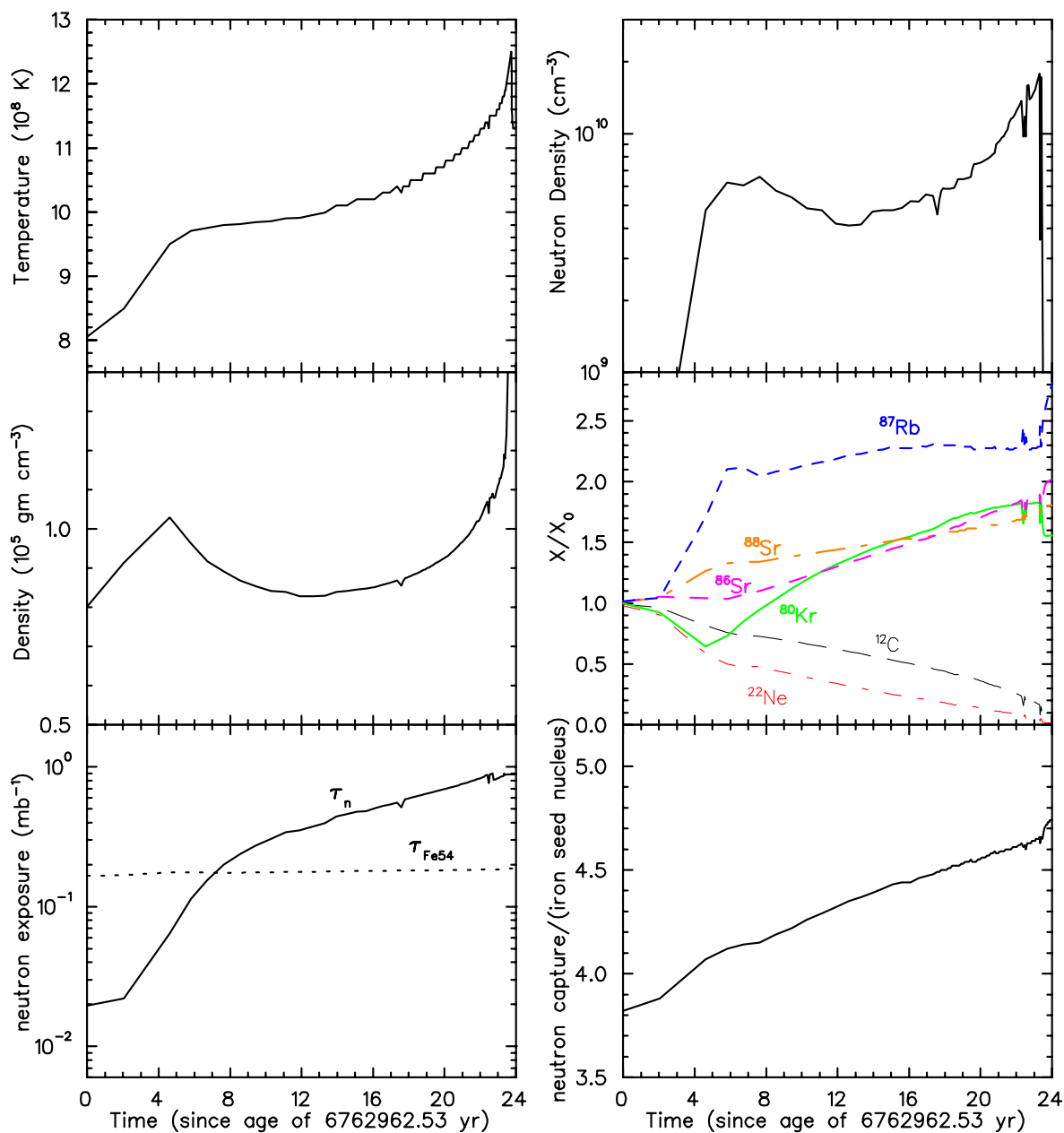


Fig. 9.— The same as Fig. 8 for the sequence 25K. The quantities are taken at a mass coordinate $M_r=1.38 M_\odot$, which is the location of the bottom of the carbon-burning shell in this model. Note the gradual increase of the neutron density following the gradual change of temperature and density.

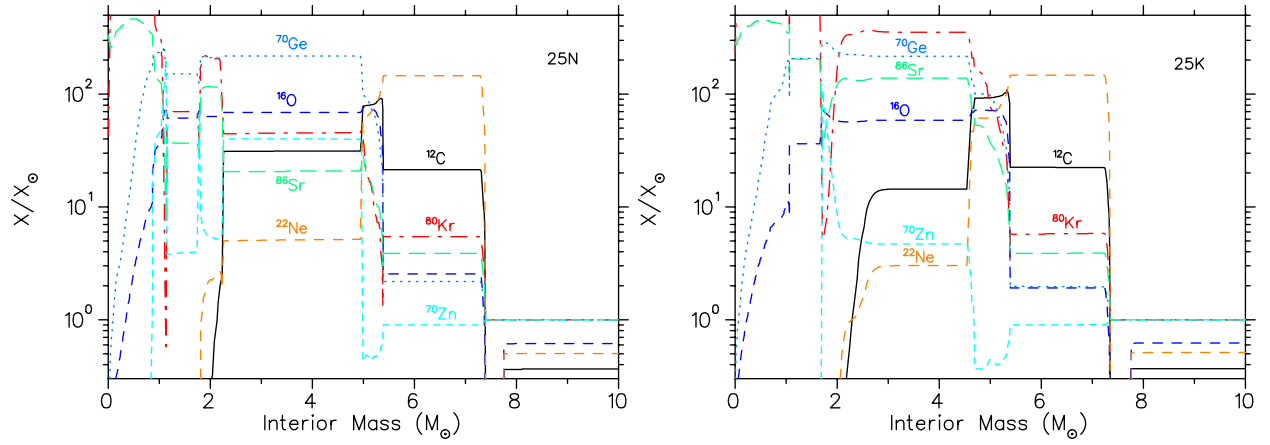


Fig. 10.— Mass fractions of various important nuclear species normalized to solar values versus interior mass. These curves represent snapshots at the end of oxygen burning in a 25 M_{\odot} star for model sequences 25N and 25K.

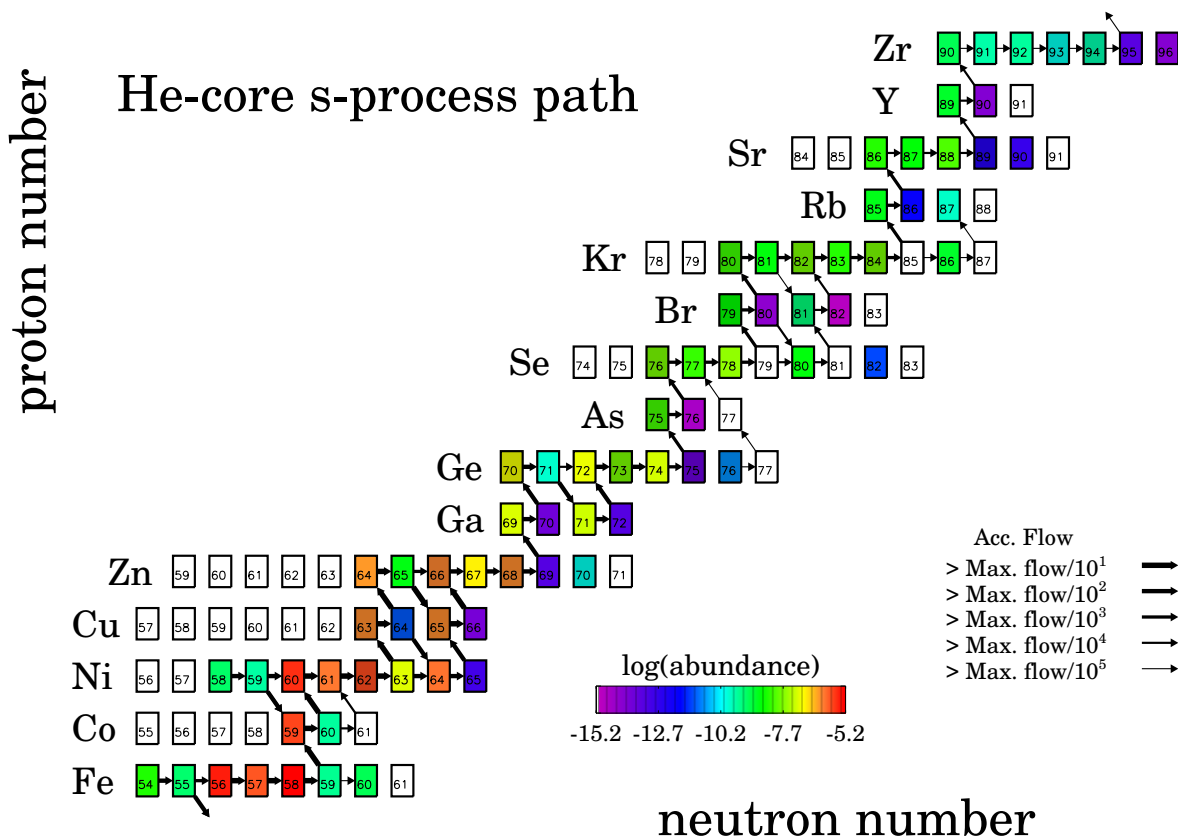


Fig. 11.— s-process nuclear reaction flow and final abundance for the s-process during core He-burning in a one-zone nucleosynthesis calculation using the central temperature, density, and ${}^4\text{He}$ mass fraction tracks of our evolutionary sequence 25N. The thickness of an arrow shows the level of that reaction flow (i.e. $\sum_n N_A \langle \sigma v \rangle \rho y_i y_j dt_n$) relative to the maximum reaction flow within the boundary of the chart. The largest neutron-capture flows within the range of the figure are the ${}^{56,57,58}\text{Fe}(n,\gamma)$ reactions.

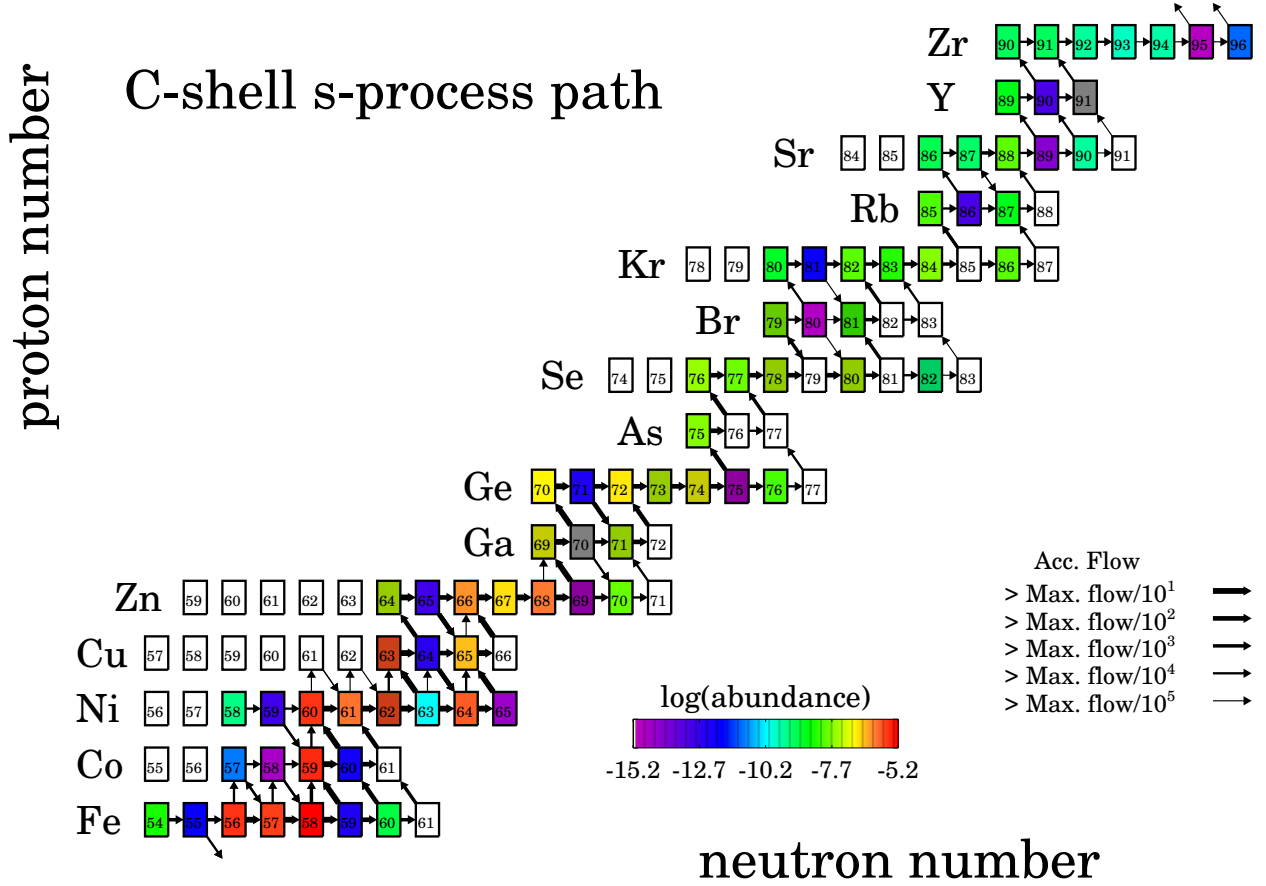


Fig. 12.— Chart of nuclear reaction flow for the s-process during shell carbon burning in one-zone calculation using the temperature, density, and ^{12}C mass fraction tracks of the innermost shell of convective C-burning of our evolutionary sequence 25N. The largest neutron-capture flows within the range of the figure are $^{58}\text{Fe}(n,\gamma)$, $^{57}\text{Fe}(n,\gamma)$, and $^{56}\text{Fe}(n,\gamma)$ reactions. The largest proton-capture flows within the range of the figure are the $^{58}\text{Fe}(p,g)$, $^{57}\text{Fe}(p,g)$, and $^{56}\text{Fe}(p,g)$ reactions. The largest neutron-producer reactions are the $^{22}\text{Ne}(\alpha,n)$, $^{21}\text{Ne}(\alpha,n)$, $^{17}\text{O}(\alpha,n)$, $^{13}\text{C}(\alpha,n)$, and $^{26}\text{Mg}(\alpha,n)$. The ratios of their relative strengths are 0.60:0.19:0.15:0.03:0.03, respectively.

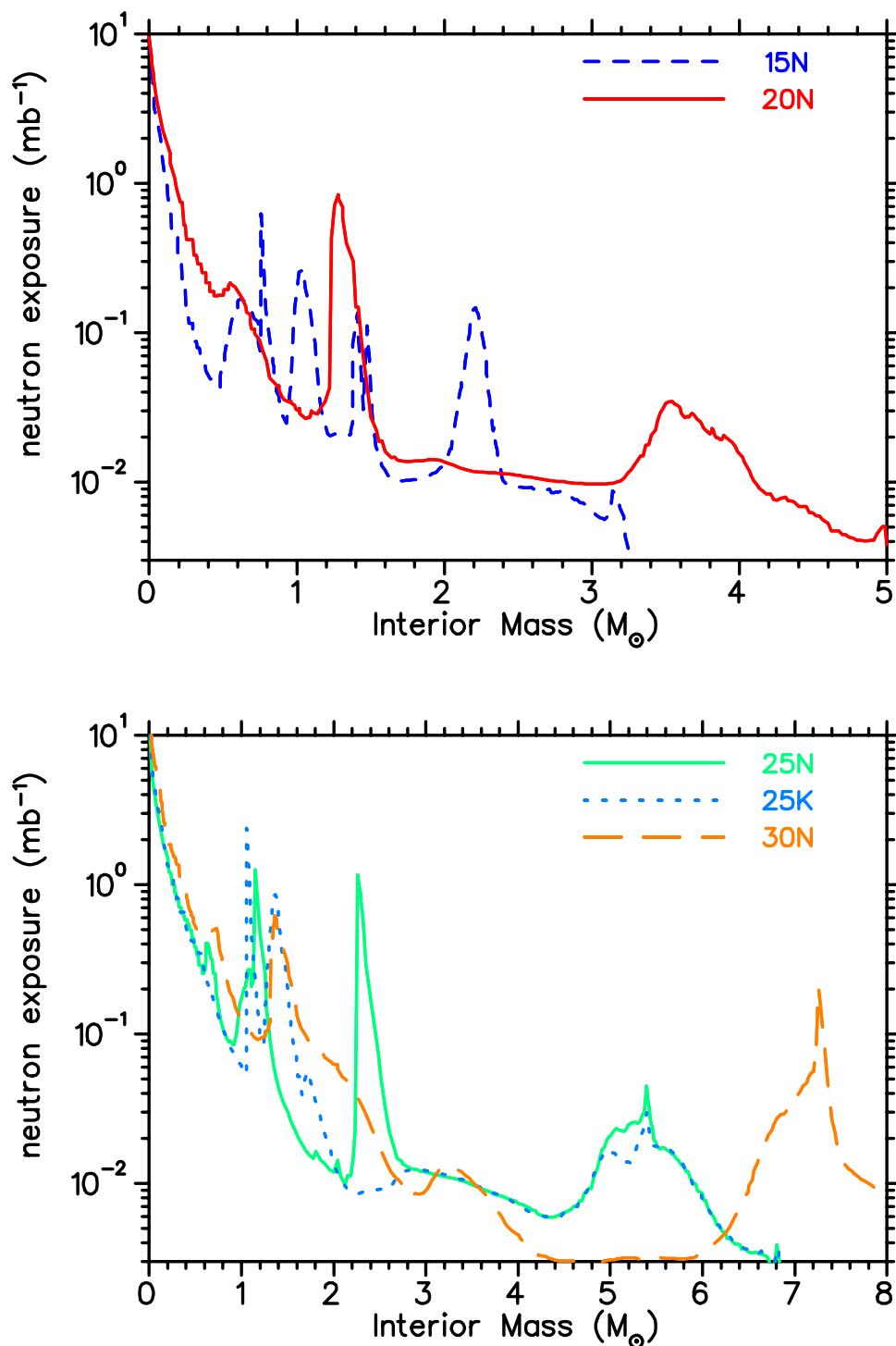


Fig. 13.— Neutron exposure versus interior mass for sequences 15N, 20N, 25N, 25K, and 30N taken at the end of core oxygen burning. The curves indicate the history and the location of s-process nuclear burning in the stellar models. The baselines of the curves are due to the s-processing during core helium burning with their highest values at the central region of the models. The narrow peaks superimposed on the generally falling curve arise from neutron exposure during different phases of shell carbon burning, except the outermost broad peak, which is due to the neutron exposure in the helium-burning shell (see also Table 5).

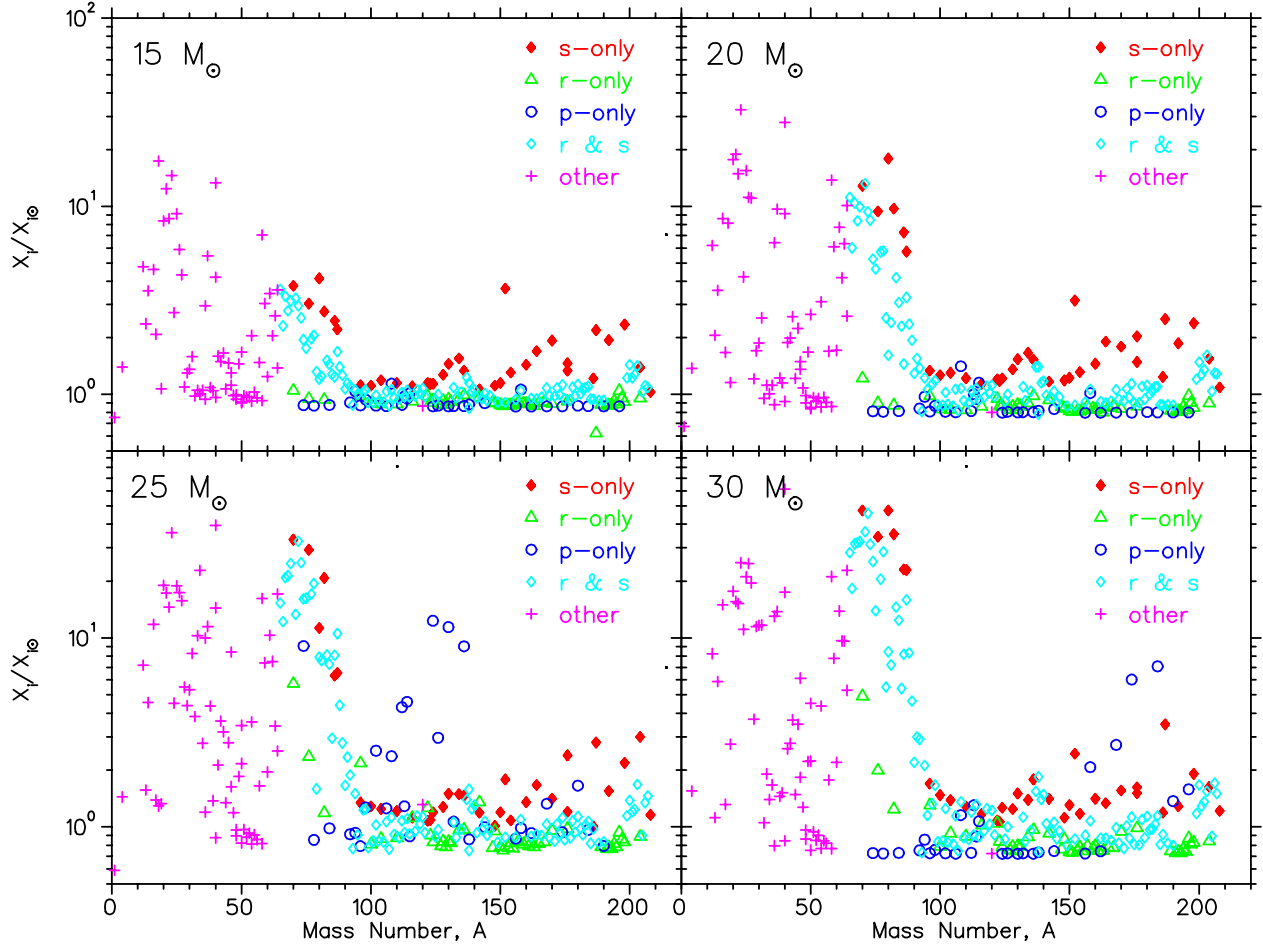


Fig. 14.— The overproduction factor distribution averaged over the ejecta of models 15N, 20N, 25N, and 30N.

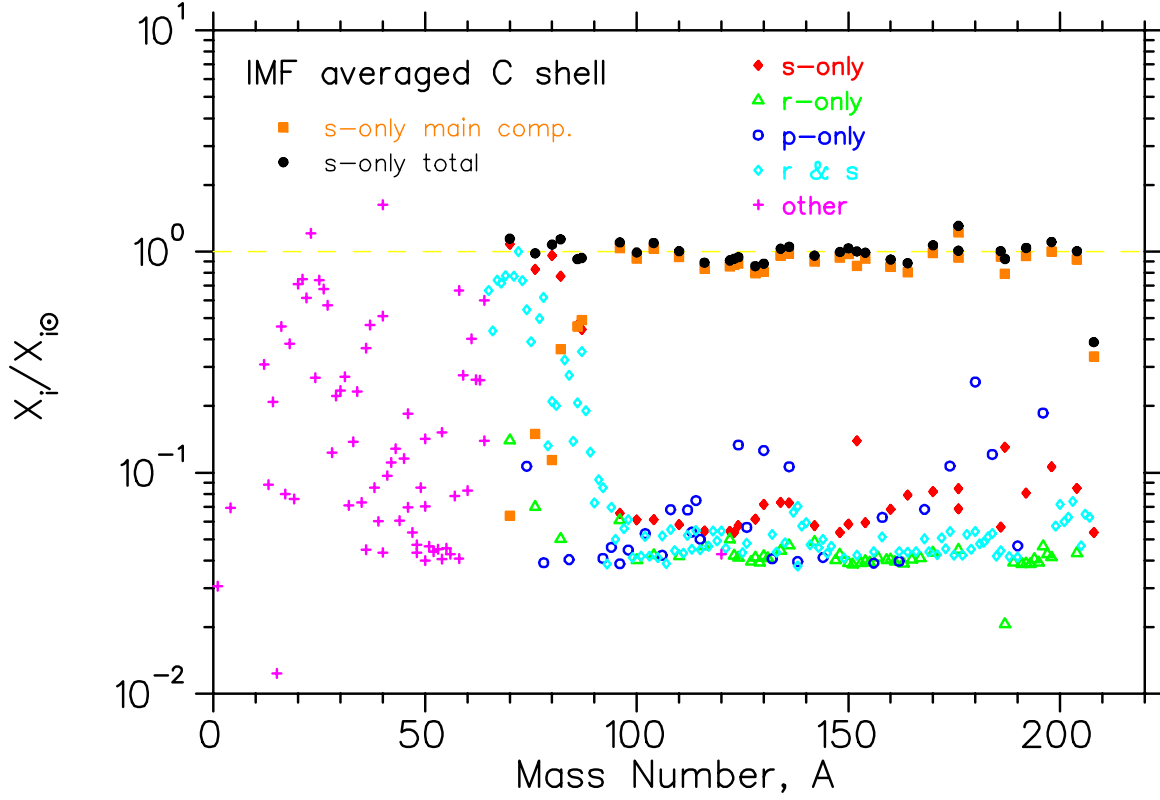


Fig. 15.— The overproduction factor distribution of the IMF-averaged of models 15N, 20N, 25N, and 30N that gives best fit to the s-only nuclei solar distribution after adding the s-only from the main component to the weak component. The χ^2 of the best fit is 153 with 32 degrees of freedom. The primary nucleosynthesis production process for each nuclei is indicated by the symbol type. The s-only contribution from the main component is shown with solid squares. The s-only contribution from the weak component is shown with solid diamonds and the total s-only abundance of the weak and main component is shown with solid circles. The dashed line represents the solar abundance distribution. Note that we only include the s-only nuclei of the main component in the plot.

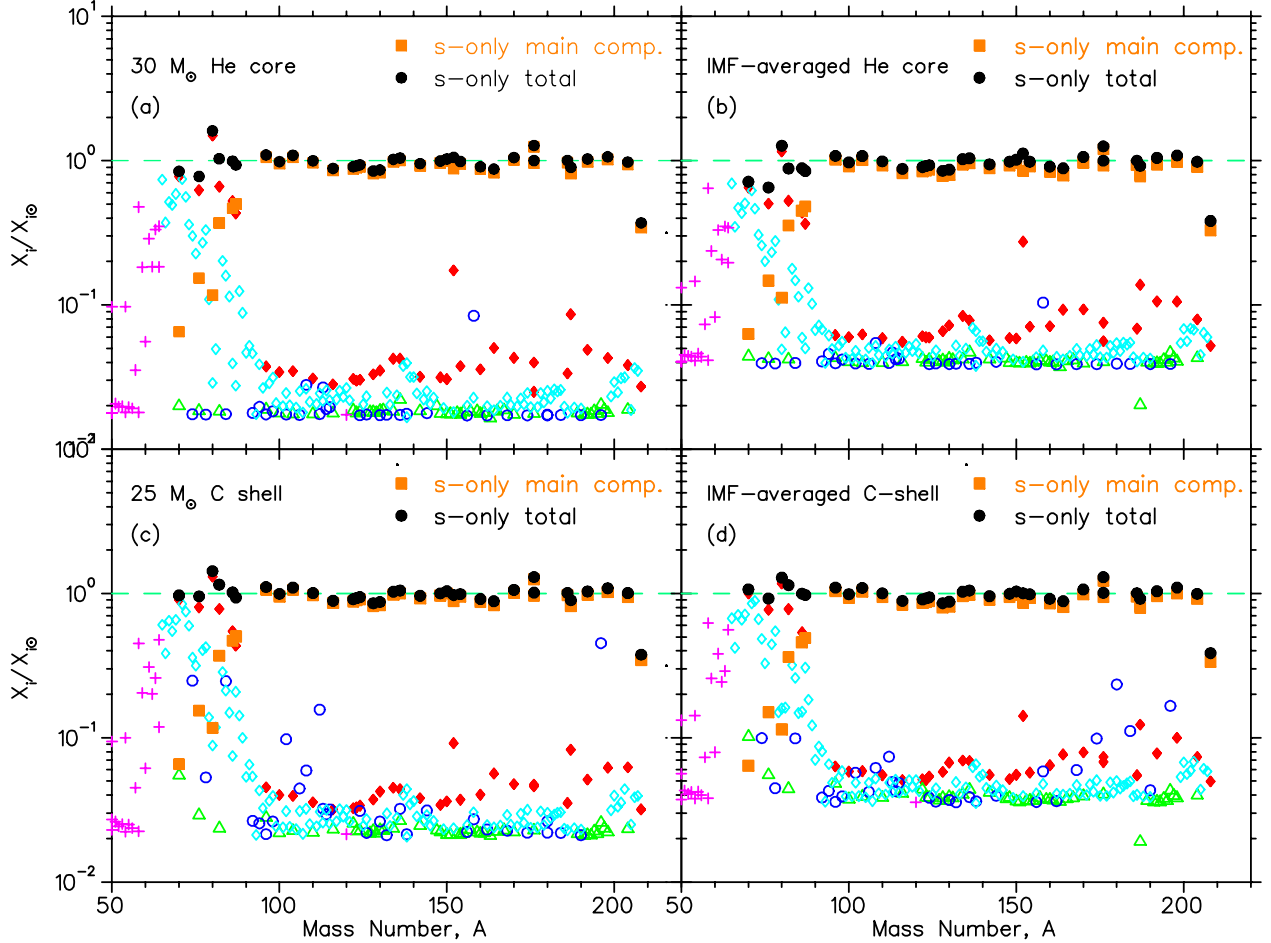


Fig. 16.— Similar to Fig. 15 but for model 30N at the end of core helium burning ($\chi^2=176$ see text, panel a: top left), for the IMF-averaged of models 15N, 20N, 25N, and 30N at the end of core helium burning ($\chi^2=205$, panel b: top right), for model 25K at the end of core oxygen burning ($\chi^2=161$, panel c: bottom left), and for the IMF-averaged of models 15N, 20N, 25K, and 30N at the end of core oxygen burning ($\chi^2=153$, panel d: bottom right). The improvement of the fits going from s-only product of the core helium burning to the product of shell carbon burning shows the importance of including s-process nucleosynthesis from shell carbon burning in fitting the solar abundance. Also averaging the overproduction factors over the stellar mass range is necessary to fit the solar abundance distribution. The small spread of overproduction factor, $X_i/X_\odot > 0.5$ for nuclei with $60 \leq A \leq 90$ suggests that solar abundance nuclei in this mass range are dominantly produced by the s-processing in massive stars (see also Table 8).